University of Cincinnati

Date: 2/27/2020

I, Karthik Vigneshwar Cuddalore Balakumar M.S., hereby submit this original work as part of the requirements for the degree of Master of Science in Aerospace Engineering.

It is entitled:

Analysis of Energy Separation in Vortex Tube using RANS based CFD

Student's name: **Karthik Vigneshwar Cuddalore Balakumar M.S.**

This work and its defense approved by:

Committee chair: Peter Disimile, Ph.D.

Committee member: Shaaban Abdallah, Ph.D.

Committee member: Milind Jog, Ph.D.

36574

Analysis of Energy Separation in Vortex Tube using RANS based CFD

A thesis submitted to the graduate school of the University of Cincinnati in partial fulfillment of the requirements for the degree of

MASTER OF SCIENCE

In the Department of Aerospace Engineering and Engineering Mechanics of the College of Engineering & Applied Sciences

February 27th, 2020

By

Karthik Vigneshwar Cuddalore Balakumar
B.E. Anna University, 2015

Committee chair: Dr Peter J. Disimile
Dr. Shaaban Abdallah
Dr. Milind A. Jog

Abstract

In the current thesis, an analysis of energy separation in a Ranque-Hilsch Vortex Tube (RHVT or simply VT) using results from CFD has been performed. Initially the 3D CFD model of the VT was validated against published experimental data and was found to have a very good agreement in terms of total temperature predictions at the hot and cold outlets. The flowfield in the VT was analyzed using RANS based two-equation turbulence model $Std\ k-\epsilon$. Comparisons were made between a published LES research to get an idea of how the turbulence models differed in their predictions of highly swirling flows like the vortex tube flow which exhibit an anisotropic behavior with respect to turbulence production and the stresses resultantly. The velocities were studied in detail to define the free and forced vortex regions which are found in swirling flows and also to define the cross-over region between the two counter-flowing streams of hot and cold fluid where turbulent stresses and generation of turbulence are expected to be maximum. The turbulence generated at the cross-over region breaks down in the annular region affected by viscosity near walls which causes the turbulence breakdown to heat neat the walls and thus the hot temperature.

Next, the other flow properties like the static and total temperatures, vorticity, strain rate and Reynolds stresses inside the VT were studied in detail using the results from the CFD simulation which would have been otherwise very difficult to obtain using experimental techniques. In the further analysis, it was found that there is a flow of energy in the form of work and heat from the core flow to the annular flow region which causes the core flow temperature to drop and that of the annular flow to increase. A control volume (CV) analysis was performed with the cold flow forming the control volume and the CV boundary being defined by the cross-over region between the cold and hot flow. The calculations were in very good agreement with the assumptions made regarding the heat and work

transfer. The analysis revealed that the shear work was the dominant mode of work transfer, which was performed by the cold flow on the hot flow and also a presence of turbulent heat conduction due to the eddies away from the core flow. The heat transfer was found to be only a fraction of the shear work transfer that is present.

Acknowledgement

To my parents who were brave enough to send their only son to pursue Master's on the other side of the world.

This thesis wouldn't have been possible without the support of my mentor Dr.Peter J Disimile who believed in me and gave me an opportunity to work under him in his lab. Thank you for the guidance and showing us how to conduct research, the importance of documentation in any activity because of which the writing of this final thesis was far easier than it would've been to combine all the data and analysis later on.

My most cherished days during my Master's would be those when I was a part of the HyperloopUC team working on the fifth mode of transportation and I will always be thankful for this wonderful opportunity which taught me a lot technically and also made me realize the value of soft skills. Going to the SpaceX facility to showcase our version of the Hyperloop Pod was an experience that would always be close to my heart.

I would also like to extend my gratitude to my lab mates Sanjay, Viswa, Dhaval, Raj, Akshay and Qasim with whom I have had very many conversations about my research and fluid mechanics which helped a lot in clarifying some of the concepts which were difficult to understand at first.

Finally, I would like to thank the Graduate Department of Aerospace Engineering at the University of Cincinnati for providing me the opportunity to pursue my Master's with a scholarship which eased the financial burden and enabled me to pursue my research diligently without any rush.

Table of Contents

Abstract **I**

Acknowledgements

List of Figures

List of Tables

Nomenclature

Overview

1. Introduction **1**

2. Operation of Vortex Tube **3**

3. Previous Studies on Vortex Tube **5**

4. Computational Methodology **14**

4.1. Geometry Creation 14

4.2. Mesh Generation 16

4.3. Computational Technique 21

4.3.1. Choice of Turbulence model 22

4.4. Pre-Processing 23

4.4.1. Solver Type 23

4.4.2. Boundary Conditions 25

4.4.3. Convergence Monitors 25

4.5 Post-Processing 26

5. Validation 27

6. Choice of Grid for Analysis 29

7. Grid Sensitivity 30

8. Analysis 33

8.1. Comparison with LES Research 33

8.1.1 Comparison of Tangential Velocity Profiles 33

8.1.2. Comparison of Axial Velocity Profiles 37

8.1.3. Comparison of Static Temperature Profiles 39

8.1.4. Observations 41

8.2 Analysis of flow properties 42

8.2.1. Velocity Analysis 43

8.2.2. Vorticity and Strain Rate 48

8.2.3. Reynolds Stress 52

8.2.4. Energy Contained in the Flow 59

8.3. Analysis of Cold Flow 65

8.3.1. Control Volume Analysis of Cold Flow 67

8.3.2 Calculating Heat and Work Transfers 71

9. Conclusion and Future work **77**

References

List of Figures

Figure 1. Streamline in a Counter Flow Vortex Tube obtained from current CFD (scan QR code for animation) 2

Figure 2. Commercial Vortex tube with different parts from Exair Corp. 3

Figure 3. Concept of multi-circulation envisioned by Xue et al. [3] 6

Figure 4. Concept of Görtler Vortices on the Vortex tube wall [18] 8

Figure 5. Vortex tube dimensions 15

Figure 6. Law of the Wall [31] 18

Figure 7. Unstructured mesh (top), Structured mesh (bottom) with low quality elements marked .. 20

Figure 8. Density-based Solver [25] 24

Figure 9. Hot temperature difference Vs Cold mass fraction 27

Figure 10. Cold temperature difference Vs Cold mass fraction 28

Figure 11. Grid sensitivity analysis 31

Figure 12. Reynolds stress at various axial locations for different grid sizes 32

Figure 13. Normalized tangential velocity at x=36 mm 35

Figure 14. Normalized Tangential Velocity at x=56 mm 36

Figure 15. Normalized Axial Velocity at x=36 mm 38

Figure 16. Normalized Axial Velocity at x=56 mm 39

Figure 17.Normalized Static Temperature at x=36 mm 40

Figure 18. Normalized Static Temperature at x=56 mm 41

Figure 19. The stations at which the results are studied 42

Figure 20. Tangential velocity distribution at various axial locations 44

Figure 21. Tangential velocity distribution at various axial locations 46

Figure 22. Axial velocity cross-over locations at various locations 47

Figure 23. Vorticity (left), Strain (right)..... 49

Figure 24. Axial vorticity or Vorticity X at various locations..... 50

Figure 25. Strain rate at various axial locations..... 51

Figure 26. Eddy viscosity at various axial locations..... 55

Figure 27. Reynolds Stress at various axial sections 56

Figure 28. Reynolds Stress and axial velocity at various axial locations 58

Figure 29. Static Temperature distribution at various axial locations..... 60

Figure 30. Total Temperature distribution at various axial locations 61

Figure 31. Total temperature contour inside the vortex tube 61

Figure 32. Total Energy distribution at various axial locations..... 63

Figure 33. Total Temperature at Vortex tube periphery..... 64

Figure 34. Hot flow just outside the inlet section..... 66

Figure 35. Static Temperature at the centerline of the vortex tube..... 67

Figure 36. Control Volume of Cold Flow..... 68

Figure 37. Planes to calculate the entrained mass..... 70

Figure 38. Temperature Gradient in y-direction at different axial locations..... 72

List of Tables

Table 1. Dimensions of the Vortex Tube 15

Table 2. Boundary conditions for the current CFD model 25

Table 3. Calculating of the flow energy entering and leaving the control volume 70

Table 4. Calculating of the work and heat transfer at the control surface 74

List of Symbols

Symbol	Description	Units
L	Vortex tube length	m
D	Vortex tube diameter	m
y	Radial Coordinate	-
R	Radius of Vortex tube	m
k	Turbulence Kinetic Energy	m^2/s^2
u, v, w	Mean velocities in x, y & z-directions	m/s
u', v', w'	Fluctuating velocities in x, y & z-directions	m/s
V	Velocity magnitude	m/s
ex	Exergy	J/kg K
h	Enthalpy	J/kg K
$\dot{Q}$	Rate of heat transfer	W
$\overline{u_i' u_j'}$	Reynolds Stress	Pa
$\dot{W}$	Rate of work transfer	W
$\dot{m}$	Mass flow rate	kg/s
E_{CV}	Energy inside the CV	W
C_p	Specific heat at constant pressure	J/kg K
$C_{1\epsilon}$, $C_{2\epsilon}$, $C_{3\epsilon}$, σ_k & σ_ϵ, C_μ	Turbulence model constants	-
Greek Letters		
ρ	Density	kg/m^3
g	Acceleration due to gravity	m/s^2

ϵ	Rate of Dissipation	m^2/s^3
ω	Specific rate of dissipation	1/s
μ	Molecular viscosity	kg/m s
μ_t	Turbulent viscosity	Pa s
λ_t	Turbulent Heat Conduction, μ_t/Pr_t	Pa s
ε	Cold mass fraction, $\dot{m}_c/\dot{m}_i$	-
Θ	Exergy Density	-
δ_{ij}	Kronecker delta	-
ϕ	Rate of viscous dissipation	N/m^2 s
τ	Shear stress	N/m^2
γ	Specific heat ratio	-

Subscripts & Accents

t	Turbulent properties
T	Total properties
i	Indices
overbar	Time-averaged properties

Acronyms & Abbreviations

CFD	Computational Fluid Dynamics
RHVT	Ranque-Hilsch Vortex Tube
VT	Vortex Tube
RANS	Reynolds Averaged Navier Stokes
LES	Large Eddy Simulation
SST	Shear Stress Transport

RNG	Re-Normalization Group
Std	Standard
DOE	Design of Experiments

Overview

1. C. B. Karthik Vigneshwar and D. J. Peter, "CFD ANALYSIS OF TURBULENT SWIRLING FLOW CHARACTERISTICS IN A RANQUE-HILSCH VORTEX TUBE USING A RANS BASED TURBULENCE MODEL," *Int. J. Eng. Sci. Res. Technol.*, vol. 8, no. 1, pp. 74–99, 2019.

1. Introduction

Maxwell's demon is a well-known paradox in thermodynamics. It refers to a system where there are two containers separated by a diaphragm. Both containers contain gas at a particular temperature. The paradox is about a magical force which is referred to as the demon (hence the name Maxwell's demon) which opens the diaphragm and allows only fast-moving molecules to pass to the other side, the right chamber and slow-moving molecules to migrate into the left chamber. Thus, after some time, the fast moving and slow-moving molecules would have been separated. Since fast moving molecules cause static temperature rise and slow-moving molecules cause temperature drop, this means that heat is flowing from a cold to a hot body causing a corresponding drop in system entropy. This is in direct contradiction to the Second Law of Thermodynamics which states that the entropy of a system should always increase which means heat should always flow from a hot to a cold body and both should eventually reach an equilibrium state with passage of time. In a vortex tube a similar result occurs. A vortex tube is a simple mechanical device without any moving parts which splits incoming tangentially injected air stream into two separate streams, one flowing at the periphery of the tube (i.e., the annular flow) and the other flowing in the core of the tube, with the annular flow being hotter and the core flow being colder than the inlet as it exits the vortex tube exit. Thus, an energy separation happens by means of some flow mechanisms which act like a demon in this case and this happens without any moving parts or complicated device geometry. In order to achieve this temperature separation, the vortex tube inlet has to be supplied with a compressed gas and since compressed air doesn't come cheap, the COP (Coefficient of Performance) of the vortex tube is less when compared to the more widely used vapor compression cycle in air conditioners, thus limiting the use of vortex tubes to situations where compressed air is readily available. Some examples where compressed air is readily available would be machine shops and other heavy industries where vortex tubes are used for spot

cooling of the tool bits in lathes, food industry and in places where reliability and serviceability (vortex tubes require no servicing since it has no moving parts) are key, like space vehicle applications. Thus, increasing the COP of vortex tubes is beneficial and in order to do this, the fundamental mechanism causing this energy transfer has to be understood. This has been the research focus for the past 85 years on vortex tubes, ever since its invention in the year 1931 by Georges J. Ranque.

Figure 1. Streamline in a Counter Flow Vortex Tube obtained from current CFD (scan QR code for animation)

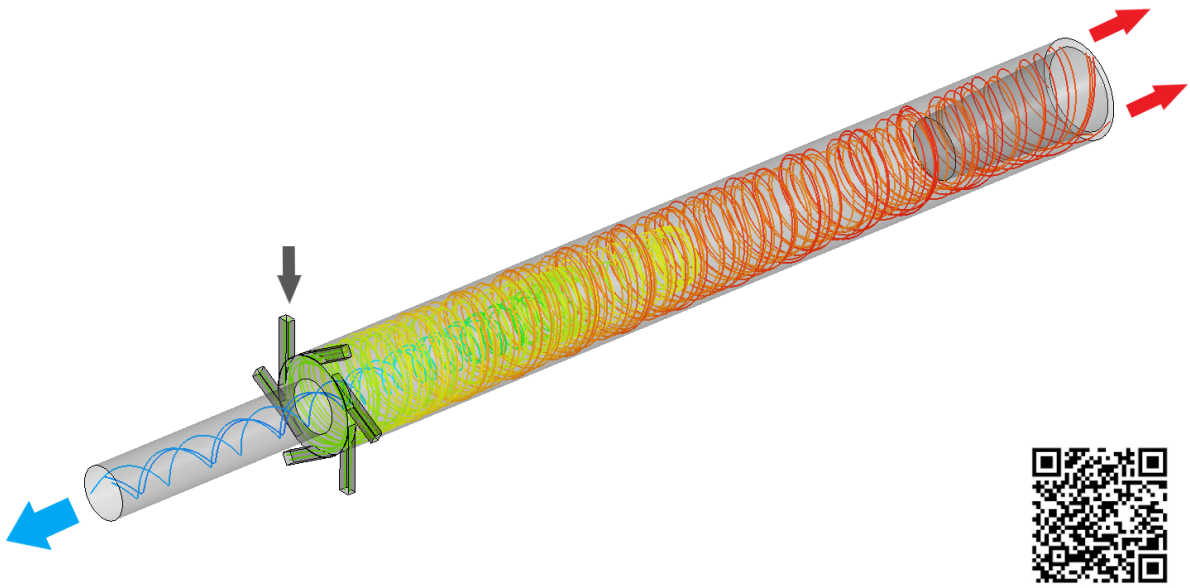

The two main types of vortex tubes are the parallel and counter flow Vortex tube. As the name suggests, in a parallel flow vortex tube, the two fluid streams (outer and the core) flow in the same direction along the vortex tube. In a counter flow design, the two streams flow in opposite directions and exit the vortex tube from two exits situated on the opposite ends of the tube. Extensive researches have been done on both types of vortex tubes and counter flow design was found to be the more efficient and hence the most widely used of the two.

2. Operation of Vortex Tube

The Vortex tube has 4 components. They are (i) Swirl chamber with the inlets (ii) Vortex tube main chamber (iii) Hot exit valve & (iv) Cold orifice.

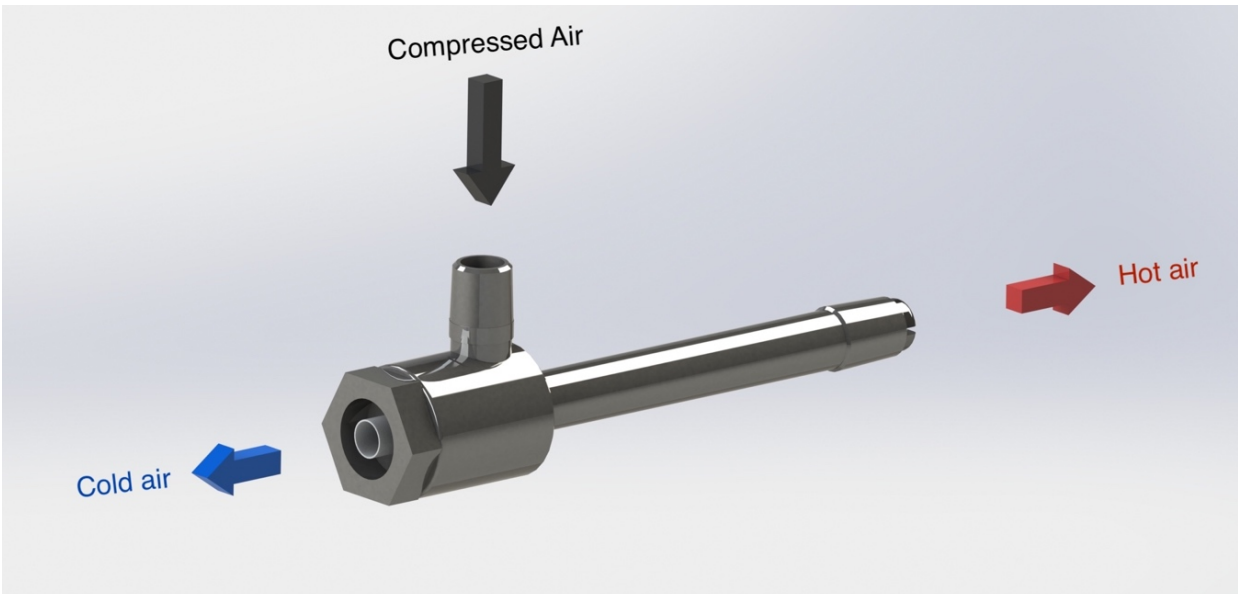

Figure 2. Commercial Vortex tube with different parts

Compressed air is supplied at the inlet. This air enters the swirl chamber where the flow gets converted to a swirl flow with a high Swirl number $\left(S = \frac{Axial\ flux\ of\ angular\ momentum}{Axial\ flux\ of\ axial\ momentum}\right)$ flowing along the vortex tube wall. Some flow also enters the center of the vortex tube. The two exits of the vortex tube, the Hot and the Cold exit are maintained at different pressures. The cold exit is generally open to atmosphere and the hot exit has a conical valve that can be adjusted to control the pressure at the hot end and thus controlling the mass flow rate of the air leaving the exits. The variable is usually denoted by the term cold mass fraction (ε) which is the ratio of the mass flow rates at cold exit to the mass flow rate at the inlet $(\dot{m}_c/\dot{m}_i)$. Thus, adjusting the control valve one can adjust the cold mass fraction

(ε) of the vortex tube and subsequently the heating or cooling capacity of the vortex tube (temperatures also vary with the cold mass fraction).

3. Previous Studies on Vortex Tube

One of the earliest experimental investigations on a vortex tube was done by J.P. Harnett & E.R.G Eckert [1]. Here the authors measured the component velocities (u, v & w), total temperatures and pressures at various axial locations inside a relatively large vortex tube. Comparison was done between swirl flows in vortex tube and other types of flows such as Couette flow and Poiseuille flow (with and without rotation) to highlight the parameters important for energy separation. Brunn [2] also performed an experimental investigation, but with higher fidelity using different measurement devices and acquired data at more axial locations inside the vortex tube. Deissler and Perlmutter [3] did extensive analytical research on compressible turbulent swirling flow in vortex tubes and concluded that total temperature rise in the annular region was because of the shear work done by the expanding fluid as it moves towards the center of the tube which in turn causes the fluid in the core to lose its energy. They also calculated the energy dissipation and found it to be the dominant mechanism responsible for the temperature rise within the annular region. The loss of total temperature in the core region was correlated to the loss of kinetic energy and pressure in that region. Van Deemter [4] analytically examined flow in a vortex tube and concluded that in a turbulent swirling flow with a uniform angular velocity, the temperature distribution would be adiabatic and hence no thermal energy transfer. But the non-uniform velocity profile in the vortex tube gives rise to a flow of mechanical work from the inner to the outer regions. In addition, there is a flow of heat from the wall to the center which counterbalances this mechanical energy and therefore the temperature of the flow deviates from an adiabatic temperature distribution. Yunpeng Xue et al. [5] experimentally examined a vortex tube and noted the presence of a forced vortex in the core of the flow, at the point of flow injection. He also found that this forced vortex gradually transformed into a free vortex as the fluid moves towards the hot exit with a multi-circulation zone between the core and peripheral flows. The

authors then calculated the exergy [6] (useful energy that can be transformed into a temperature difference) at various axial locations inside the vortex tube and plotted the exergy density ($\Theta = ex/ex_{max}$). The exergy density was found to decrease from the inlet towards the hot exit which made them further conclude that the energy separation due to internal friction (i.e., molecular) between the fluid layers was absent.

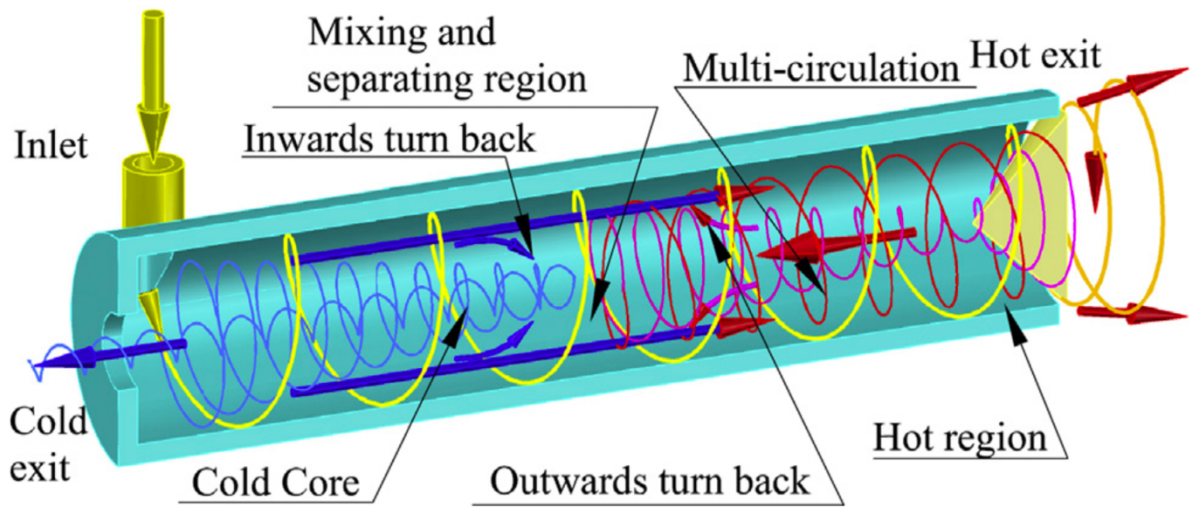

Figure 3. Concept of multi-circulation envisioned by Xue et al. [3]

Ahlborn and Stuart Groves [7] performed experiments and theorized the flow inside the vortex tube. They found two primary flows (hot and cold) with oppositely directed axial velocities and a purely azimuthal secondary flow in the region between them which acts as a medium for heat and mass transfer. They [8] then compared this secondary circulation loop to a classic refrigeration cycle and divide the secondary flow into 4 regions (i) Heat Rejection, (ii) Adiabatic Expansion, (iii) Energy Absorption, (iv) Adiabatic Compression and also derived expressions for predicting hot and cold temperatures from the pressure ratios between inlet and the outlets. Heishichiro Takahama & Hajime

Yokosawa [9] did experiments comparing the performance of vortex tubes with straight and divergent chambers. They compared the flow properties in vortex tubes with varying divergent angles & lengths and plotted them for the various sections along the axis of the vortex tube. They found that the length of a vortex tube had an impact on the performance by dropping the stagnation enthalpy of the cold stream of the vortex tube. Specifically, a vortex tube with divergent angles in the range ($\theta = 1.7 - 5.1$ deg) had the maximum efficiency and achieved this with a shorter length ($L = 38D$). The flow characteristics also changed significantly between the vortex tube with a straight chamber and one with a divergent chamber wherein a larger forced vortex region was observed in the radial direction in the vortex tube with divergent chamber. The intensity of swirl which is defined by the ratio of the angular momentum to the axial momentum was found to decrease along the direction of flow in case of straight tubes but increased with large divergent angles. P.A. Ramakrishna et al. [10] performed experiments on different vortex tube materials to study the effect of heat transfer in vortex tube because of the different thermal conductivities of the tube wall. In their experiments they found that at lower inlet temperatures of the fluid, the PVC (Polyvinyl Chloride) vortex tube had a better performance than the one made with MS (Mild Steel). This was due to the heat transfer between the ambient air and the fluid near the vortex tube inlet, where the static temperature was lower because of the expansion of the fluid into a low-pressure zone inside the swirl chamber in the vortex tube. When they increased the inlet temperature of the fluid such that after expansion the resulting temperature was close to that of the ambient temperature, both the tubes (MS & PVC) had similar performance which showed that heat transfer was a major factor affecting the performance of vortex tubes. The cold temperature was lower than the calculated isentropic expansion temperature, which led to their conclusion that an energy transfer mechanism was present between the core and peripheral flow. Stephan et al. [11] did an experimental investigation into energy separation within vortex tubes and hypothesized that the Görtler vortices which are formed when a fluid flows over a concave

surface, to be the factor responsible for the energy separation. In their experiment using an insulated and an uninsulated vortex tube, the hot temperature was higher in the insulated vortex tube configuration. They concluded that the reason for such a difference is that the fluid in the uninsulated vortex tube lost heat to the surroundings causing a reduction in the strength of the Görtler vortices. Xue et al. [12] performed flow visualization by injecting a dye and found flow reversal from the hot end control valve. This reversed flow again stagnated in the region upstream of the control valve and underwent flow reversal, reattaching with the annular flow region which continues to flow towards the hot end exit. They concluded that this structure of multi-circulation is the reason for the temperature increase at the hot end.

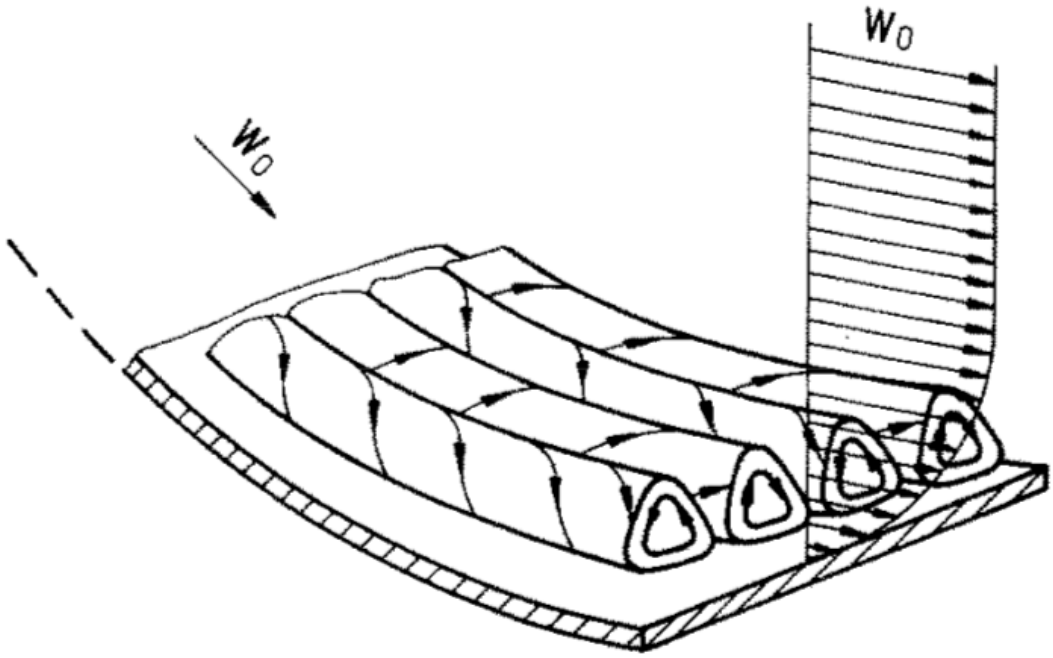

Figure 4. Concept of Görtler Vortices on the Vortex tube wall [18]

Extensive computational studies have also been performed on vortex tubes. Fröhlingsdorf & Unger [13] performed a comparison against experimental results using a 2D axisymmetric CFD model of the vortex tube. They found that when using the standard k-ε model that the eddy viscosity over predicted the tangential velocity profiles and deviated from the measured experimental values. They then used a correction factor from Keyes [14] to calculate the turbulent viscosity and the new model produced results which matched well with the experiments. Eiamsa-ard & Promvonge [15] compared the results from Algebraic Stress Model (ASM) with the experiments and found the ASM to perform better compared with $Std\ k-\epsilon$ model when comparing to the mean velocity predictions. They then tried to identify the process that has the most impact on the energy separation effect by performing calculations with just one of the energy transport terms in the energy equation and suppressing every other term. The authors found the diffusion of mean kinetic energy to play the dominant role in energy separation near the inlet of the vortex tube and also in the core region. They also found the impact of pressure work and stress production on energy separation to increase towards the hot exit away from the inlet. T. Dutta et al. [16] compared different turbulent models and found the $Std\ k-\epsilon$ to work better in terms of temperature predictions as the results were close to experimental values and $SST\ k-\omega$, $Std\ k-\omega$ and also obtained results which were slightly less accurate than $Std\ k-\epsilon$. Results from $RNG\ k-\epsilon$ deviated significantly from those of the experiments in their computations. The same authors [17] further calculated the rate of heat transfer, tangential and axial shear work at various radial and axial locations in the vortex tube. Tangential shear work was found to be the driving force for energy separation inside the vortex tube. Heat transfer was found to occur radially from the outer layers of the flow to the inner fluid core as well as in the axial direction thus reducing the overall energy separation of the vortex tube. Radial shear stress was found to be negligible. They also performed simulations to study the effect of shifting the inlet across the axial direction and found that the ideal location of the inlet was close to the cold outlet. Increasing the

distance between the inlet and the cold outlet resulted in deteriorated performance. Tangential shear work was the maximum in this region between the inlet and the cold outlet. But this shear work was found to have minimum impact on the hot temperature and an increase in heat transfer in this region resulted in an increase in the cold temperature thus reducing the performance of the vortex tube. The increase in the hot exit mass fraction also resulted in a decrease in the overall temperature difference produced by the vortex tube. Bej and Sinhamahapatra [18] studied the flow physics inside a cascaded vortex tube and calculated the shear work and heat transfer in all the three directions. They also compared these terms for different cold mass fractions (ε). They concluded that the tangential shear work was the dominant mode of work transfer which decreases as we move towards the hot exit and they also state that the viscous shear was responsible for converting the kinetic energy to thermal energy near the wall. Aljuwayhel et al. [19] performed CFD and divided the hot and cold flow into two control volumes, performed energy balance and found that there is tangential shear work transfer from cold to hot flow and axial shear work and heat transfer from hot to cold flow across the control surface.

Very few papers have done computations on Vortex tube with LES (Large Eddy Simulation) model as it is very computationally expensive and for a case like vortex tube with a complex flow physics and a lot of different scales of turbulence being involved, the requirements for running successfully an LES model becomes too high. Secchiaroli et al. [20] perfomed computations on Vortex tube with LES and compared it with three different RANS models namely the RSM (Reynolds Stress Model), $RNG\ k-\epsilon$ (Renormalization Group) and the more basic Mixing length model. They found the RSM to match well with LES in terms of tangential velocity profiles and also perform better than other models in terms of axial velocity predictions. But none of the RANS models were able to capture the

non-linear profile in static temperatures that the LES predicted. For the current thesis, the results from [15] are used for comparison of the velocity and temperature profiles since in their study, the authors have used a Vortex tube of similar dimensions to the current study and also the Reynolds number at the inlet is in closer range to the current computations. Vincenzo Bianco et al. [21] compared both RSM and LES on a double circuit vortex tube. Double-Circuit Vortex tube has a secondary inlet at the hot exit with the flow coming in the opposite direction and have been found in some studies to have a better efficiency than standard tubes. In their simulations the turbulent intensity was found to be the maximum at the imaginary surface which divided the two counter-flowing streams. The total temperature contour showed that the hot temperatures were predicted on the edge of the recirculation zones towards the wall because the fluid moves from low pressure (core) to a high-pressure region (near wall region) and gets compressed which increases its enthalpy. LES also shows the core region to be dominated by large scale coherent structures and the annular region to be characterized by small scale erratic structures. Tanvir Farouk and Bakhtier Farouk [22] also performed LES and plotted particle tracks for particle leaving the hot and cold exits. It was found that the cold particle initially traveled towards hot exit before reversing and the swirl of the cold particle decreased towards the cold exit.

Most other computational studies were focused on geometrical modifications to the vortex tube and studying its effect on the temperature separation phenomenon. Rajagopalam & Disimile [23] performed an extensive computational study on the effect of geometrical modifications such as L/D ratio, number of inlets, ratio of the diameter of swirl chamber, hot exit cone valve to the diameter of the vortex tube, cold orifice diameter on the performance of the vortex tube. Thakare et al. [24] performed both experimental and CFD studies on vortex tube by varying the cold fraction (ε), number

of inlets, diameter of inlet nozzles, L/D ratio, straight & helical inlet nozzles, etc. and computed the performance of the vortex tube. They also compared the different turbulent models and concluded that the RSM (Reynolds Stress Model) works best in terms of overall agreement with the experimental results. Bramo and Pourmahmoud [25] performed a detailed study of the change in L/D ratio of the vortex tube and its effects. They also studied the effect of the L/D ratio on the location of the stagnation point. Stagnation point is the location where the axial velocity at the centerline of the vortex tube ceases to have a negative value (i.e. the flow is stops to move in the direction of the cold exit). This is the location where the maximum temperature can be observed for the flow at the periphery. The authors found that the geometry in which the stagnation point was the nearest to the hot exit produced the highest temperature difference.

More recent studies make use of Machine Learning and Artificial Neural Networks (ANNs) [26][27][28] to build a predictive model for a given vortex tube wherein results from multiple experimental runs with the independent variables inlet pressure, no. of nozzles, mass flow rates and cold fractions (ε) and the dependent variable i.e. the temperature difference at hot and cold exits are used to train the model. The model now can predict the temperature separation for any combination of these independent variables. The studies use slightly different approaches to ANNs but are able to produce results which have a good accuracy when compared to experiments.

From the literature survey it was observed that the turbulence model was the most important component of the analysis. The energy separation phenomenon is dependent on the turbulence properties of the flow within the vortex tube and the calculation of these quantities is strongly dependent on the turbulence model being utilized. RSM was found to work best for the vortex tube study as it was able to predict the temperatures and the flow properties inside the vortex tube with

good accuracy. Whereas the two-equation models like the $k-\epsilon$, $SST\ k-\omega$ & $Std\ k-\omega$ predicted temperatures with good accuracy, however, they performed poorly when predicting flow properties.

Apparent from the literature review is that explanations for the energy separation mechanism in a vortex tube has been examined using analytic, experimental, and computational approaches, and have been presented by many researchers with no clear agreement. Many researchers have hypothesized on the mechanism of energy separation in a vortex tube, yet none have looked at the basic turbulent processes responsible for the energy transfer as these are the mechanisms that one can expect to be present in high swirling turbulent flows like that found in a vortex tube. Therefore, the present study will computationally examine the vortex tube flow in light of the turbulent parameters that are responsible for energy transfer using RANS based turbulence models. The results from this simulation will then be used to examine and correlate the cause and effect of the various phenomena that occur inside the vortex tube.

4. Computational Methodology

Any CFD analysis consists of 4 major steps:

(i) Geometry creation

(ii) Mesh generation

(iii) Computational method

(iv) Pre-Processing

(v) Post-Processing

All the 4 steps in the current study and the reasons why they were done this way are discussed in detail below.

4.1 Geometry Creation

The geometry from the current mesh was created from the data from Skye et al.[29] . Within their study both experimental and computational studies of the Vortex tube were undertaken. The authors have compared the performance of vortex tube namely the hot and cold temperature with different cold mass fractions (ε). A 3D model of the geometry was created using SolidWorks 2016. Usually in CFD simulation of internal flows, the negative volume of the geometry i.e. the volume filled by the fluid is created neglecting the solid surfaces and the thickness associated with it. The same methodology is followed here, and the created geometry file was then exported to ICEM CFD for mesh generation. In the current computations, the geometry has the Origin (0,0,0) is positioned at the axis of the Vortex tube and in the plane where the Vortex tube main chamber and the cold exit tube meet. All the dimensions referenced are given from the origin.

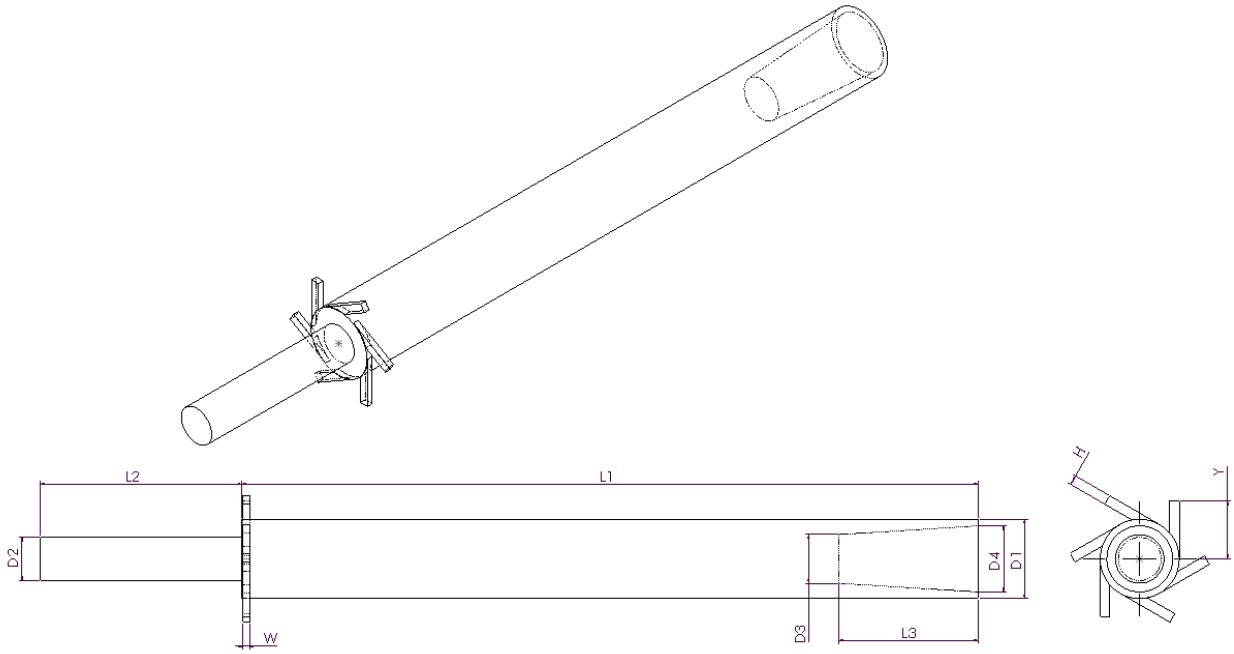

Figure 5. Vortex tube dimensions

Table 1. Dimensions of the Vortex Tube

Geometry	**Value**	**Units**
Inlet height (H)	1.41	mm
Inlet width (W)	0.97	mm
Inlet length (Y)	8.3	mm
Working tube length (L_1)	106	mm
Working tube diameter (D_1)	11.4	mm

Hot exit area (A_1)	95	mm^2
Cold exit diameter (D_2)	6.2	mm^2
Cold tube length (L_2)	29	mm
Hot end valve (D3)	7	mm
Hot end valve (D4)	9.5	mm
Hot end valve length (L3)	20	mm
No. of inlets	6	

4.2 Mesh Generation

The most crucial and time-consuming process of any CFD simulation is the mesh generation process. In any CFD simulation approximately 50 percent of the time is spent on grid generation. They are a vast array of techniques available for mesh generation and determining the best one suitable for the particular case requires a fair amount of knowledge on the different techniques. A general idea of how the solution might look based on the various features of the flow is also necessary so as to generate the mesh in the particular way, like having more number of nodes behind a bluff body in order to capture the turbulent eddy that will be generated after a particular Reynolds number.

The two types of computation mesh are: (a) Unstructured and (b) Structured. An unstructured mesh has the meshed cells randomly distributed across the flow domain. The distribution varies with different algorithms e.g. Delaunay triangulation, Octree method, Advancing front, etc. Most common

type of mesh cell used in an Unstructured mesh is a Tetrahedra although newer solvers have the option of polyhedral. A structured mesh on the other hand has the same distribution of cells from the starting face extended through the length of the domain. It is the reason why structured meshes are also called as swept meshes. Structured meshes make use of Hexahedral cells. A hybrid mesh has both the structured and unstructured meshes in the same model merged across an interface. Such a mesh was not used in the current study, but it is an area worth looking into in order to make the mesh generation process more effective.

The two types of meshes have their own advantages and disadvantages with respect to the ease of mesh generation, convergence, computational time and the results. For example, the unstructured mesh is easier to generate and saves time in the overall process as it is mostly automated but is limited in terms of the ability to be controlled and modified at specific regions in the flow domain, if needed based on the gradient of flow properties in that domain. On the contrary, a structured mesh is more difficult to generate but once generated can be easily modified wherever necessary and also a hexahedral mesh is faster and more accurate than tetrahedral mesh for the same number of nodes [30].

In the present study both the meshes were used. Initially in the validation of computational model, an unstructured mesh with polyhedral cells was used. Further when flow physics were studied in detail, a structured mesh was chosen for the same reasons mentioned above.

The two important parameters that have to be monitored for the mesh are (i) quality (ii) wall y+. The wall y+ is a non-dimensional parameter that is calculated in order to generate mesh for a particular turbulence model. Whenever there is a flow near wall, a boundary layer starts to develop. In case of a laminar boundary layer it is relatively simple, but a turbulent boundary layer has different regions. All

turbulent boundary layers follow the Law of the Wall or the Log-Law which was first found by Theodore Von Karman.

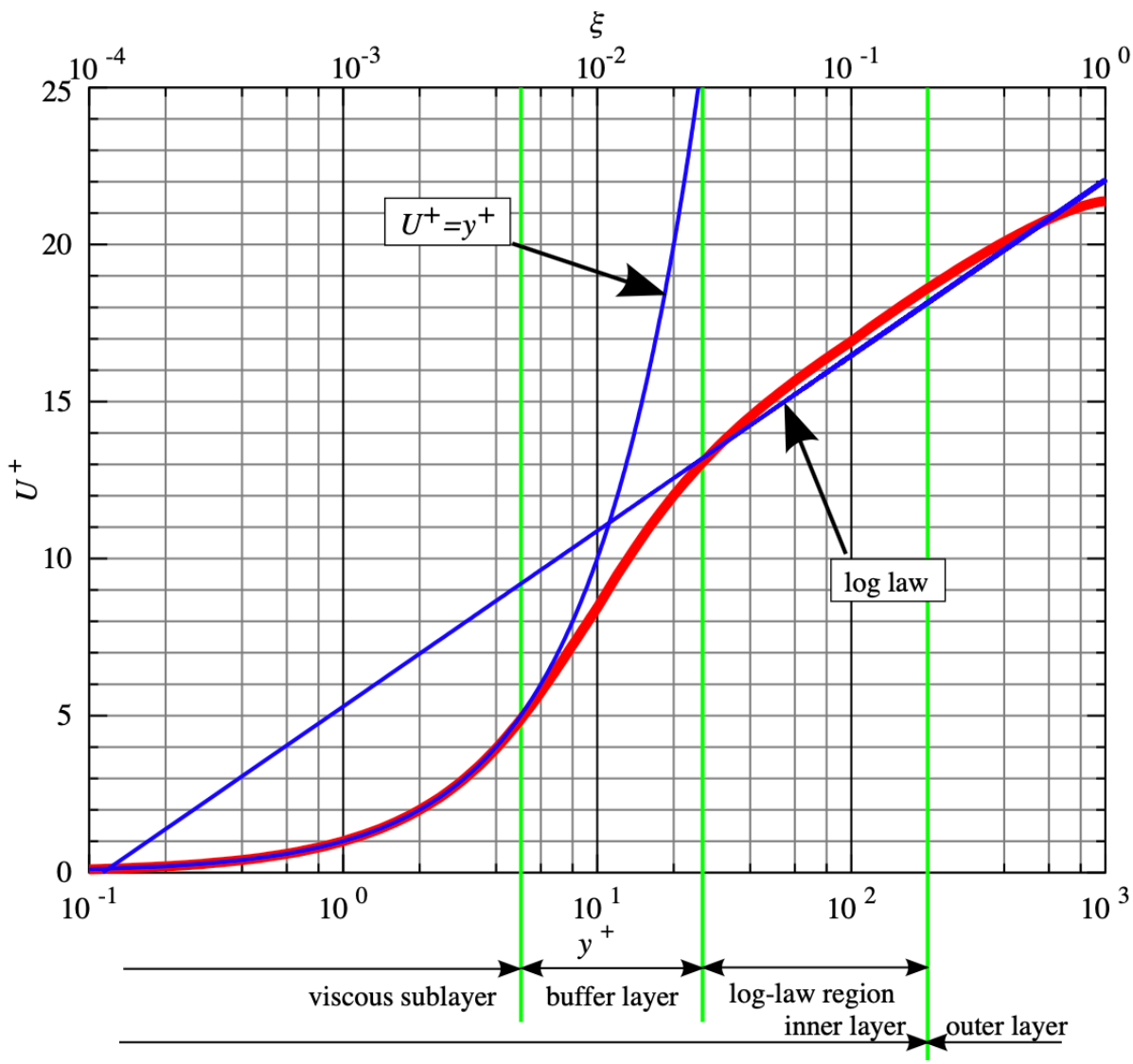

Figure 6. Law of the Wall [31]

The turbulent boundary layer has three regions. Region from 1 < y+ < 5 which is called the viscous sublayer and where the viscous forces dominate. Region from y+ > 30 is the log law region where the velocity profile follows a logarithmic profile. Region between y+ of 10 & 30 is the buffer region where

the flow transitions from a laminar sublayer to a turbulent regime. Different turbulence models have different capabilities with respect to calculating near wall turbulence. For example, some models like Spalart-Allmaras can work all the way to the viscous sublayer and hence requires a y+ of 1. Standard $k - \varepsilon$ has a default y+ requirement of more than 30. Apart from this wall functions are also used to capture near wall turbulence and different wall functions require different y+ values all of which can be obtained from standard literature. For the current simulations, $Std\ k - \epsilon$ with Standard Wall functions were used and hence a y+ of 30 was maintained.

Next is the quality of the mesh which can be monitored in numerous ways and the parameters available are extensive. Hence, only a certain quality metric which is of utmost importance in the current simulation was monitored. Firstly, the aspect ratio of the mesh was not allowed to exceed a value of 100 as the CFD solver used cannot satisfactorily handle mesh cells with an aspect ratio of more than 100. Secondly, the determinant of the mesh was maintained positive. Negative determinant means that the cells have turned inwards into themselves having negative volumes and can cause numerical issues. These issues were fairly easier to tackle in an unstructured mesh because the algorithms available in the meshing software (ICEM CFD) are pretty robust and only the sizing had to be varied in order to achieve an appropriate mesh. But in the case of a structured mesh which was done by blocking method,

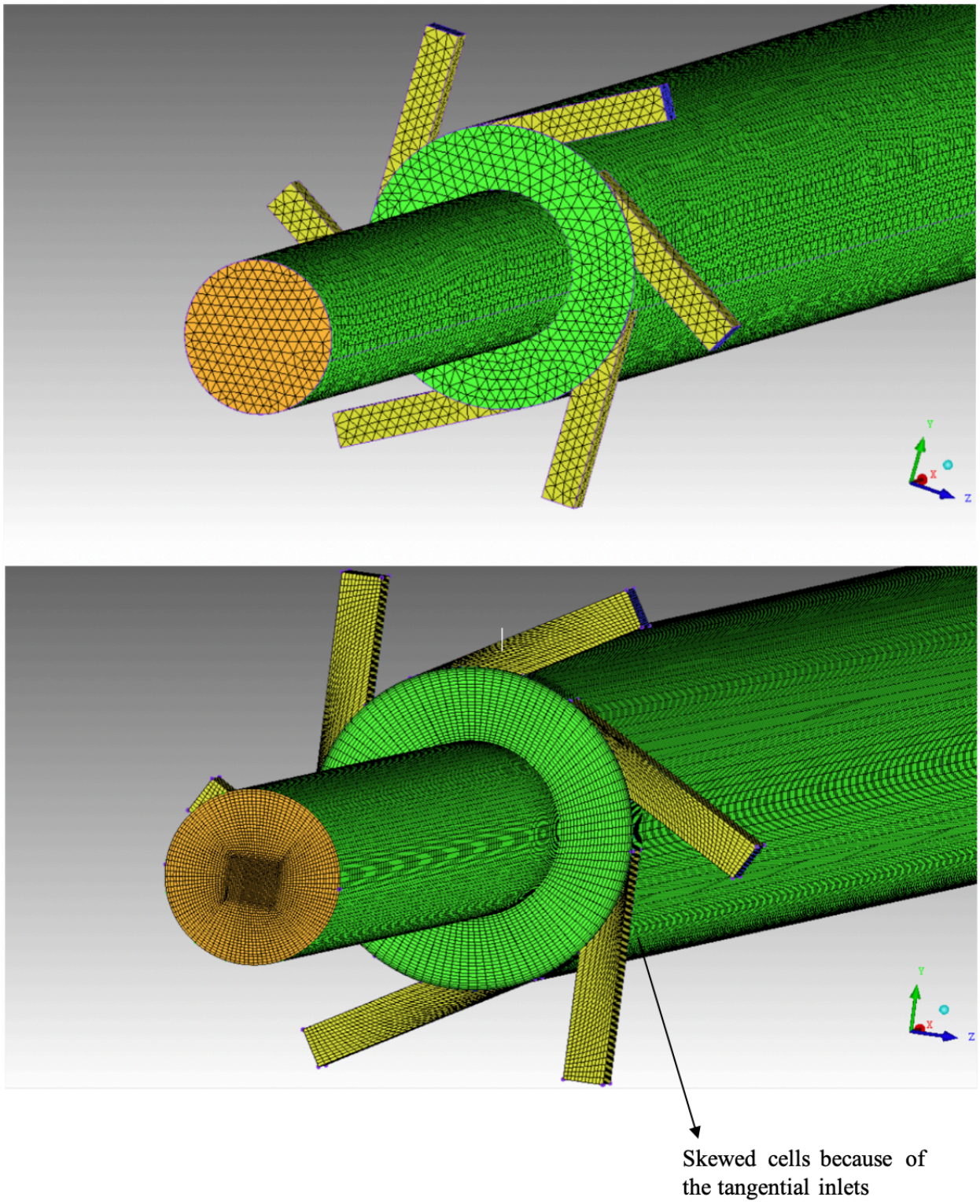

Figure 7. Unstructured mesh (top), Structured mesh (bottom) with low quality elements marked

maintaining the quality of the mesh cells was hard. It is because the blocking had to be done such that all the regions are well connected, and the blocks have to be associated to the appropriate regions. The inlets being tangential were the hardest part during the meshing process since the mesh cells at the location where the inlets met the Vortex tube chamber become highly skewed and making the mesh finer would only worsen the quality of the mesh. Thus, an appropriate node distribution had to be given in order to overcome this problem.

4.3 Computational Technique

CFD solver (ANSYS Fluent 17.1) of finite volume was used for the current simulations. In a finite volume solver, the domain is subdivided into cells and every cell subjected to three fundamental equations which govern the mass balance, momentum balance and the energy balance inside it. The momentum equations are also called as Navier-Stokes equations. The equations are given below,

$$\frac{\partial \rho}{\partial t} + \frac{\partial}{\partial x_i}(\rho \overline{u_i}) = 0 \tag{1}$$

$$\frac{\delta}{\delta t}(\rho \overline{u_i}) + \frac{\delta}{\delta x_j}(\rho \overline{u_i}\overline{u_j}) = \frac{-\delta \overline{p}}{\delta x_i} + \frac{\delta}{\delta x_j}\left[\mu\left(\frac{\delta \overline{u_i}}{\delta x_j} + \frac{\delta \overline{u_j}}{\delta x_i} - \frac{2}{3}\delta_{ij}\right)\right] \tag{2}$$

$-\overline{u_i' u_j'}$ is the unknown and it called as Reynolds Stress.

The energy equation is,

$$\frac{\partial(\rho c_p \overline{T})}{\partial t} + \overline{u_i}\frac{\partial(\rho \overline{T})}{\partial x_i} = \rho \dot{q}_g + \frac{\partial}{\partial x_i}\left(k\frac{\partial \overline{T}}{\partial x_i}\right) + \beta \overline{T}\left(\frac{\partial \overline{P}}{\partial t} + \overline{u_i}\frac{\partial \overline{P}}{\partial x_i}\right) + \phi \tag{3}$$

Where ϕ is the viscous dissipation given by,

$$\phi = \tau_{ij}\frac{\partial \overline{u_i}}{\partial x_j} = \left[-\frac{2}{3}\mu\frac{\partial \overline{u_k}}{\partial x_k}\delta_{ij} + \mu\left(\frac{\partial \overline{u_i}}{\partial x_j} + \frac{\partial \overline{u_j}}{\partial x_i}\right)\right]\frac{\partial \overline{u_i}}{\partial x_j} \tag{4}$$

4.3.1 Choice of Turbulence model

Std $k - \epsilon$ was chosen for the current simulations as it is the most widely used and robust turbulence model. In Std $k - \epsilon$ model, the Reynolds stresses are given by,

$$-\overline{u_i'u_j'} = \mu_t\left(\frac{\partial \overline{v_i}}{\partial x_j} + \frac{\partial \overline{v_j}}{\partial x_i}\right) - \frac{2}{3}k\,\delta_{ij} \tag{5}$$

Where μ_t is the eddy viscosity and it acts as the proportionality factor between the deformation tensor and the Reynolds stresses and it is given by,

$$\mu_t = \rho\, c_\mu \frac{k^2}{\epsilon} \tag{6}$$

Where C_μ= 0.09 is a constant. Other turbulence models like RNG $k - \epsilon$ specifically developed for simulation of highly swirling flows with anisotropic turbulent stresses in the form of modified eddy viscosity were considered but due to resource constraints, they were not used. k & ϵ have their own transport equations with different sets of constants that have been found by data fitting numerous

classes of turbulent flows and this is the reason why these models are also called as semi-empirical models. The transport equations of k & ϵ are given below:

$$\frac{\partial}{\partial t}(\rho k) + \frac{\partial}{\partial x_i}(\rho k \overline{u_i}) = \frac{\partial}{\partial x_j}\left[\left(\mu + \frac{\mu_t}{\sigma_k}\right)\frac{\partial k}{\partial x_j}\right] + P_k + P_b - \rho\epsilon - Y_M + S_k \tag{7}$$

$$\frac{\partial}{\partial t}(\rho \epsilon) + \frac{\partial}{\partial x_i}(\rho \epsilon \overline{u_i}) = \frac{\partial}{\partial x_j}\left[\left(\mu + \frac{\mu_t}{\sigma_\epsilon}\right)\frac{\partial \epsilon}{\partial x_j}\right] + C_{1\epsilon}\frac{\epsilon}{k}(P_k + C_{3\epsilon}P_b) - C_{2\epsilon}\rho\frac{\epsilon^2}{k} + S_\epsilon \tag{8}$$

Where P_k term represents the production of turbulent kinetic energy and P_b represents the effect of buoyancy. $C_{1\epsilon}$, $C_{2\epsilon}$, $C_{3\epsilon}$, σ_k & σ_ϵ are constants and have the values of 1.44, 1.92, -0.33, 1.0, 1.3 respectively.

4.4 Pre-Processing

The pre-processing process involves the following steps:

4.4.1 Solver Type

Since the flow inside the vortex tube is represented by a high swirl number, it falls in the category of subcritical flows where the downstream flow conditions have a significant effect on the flow upstream [32] . Hence a Density-based, implicit solver was chosen as it uses direct matrix inversion and solves for variables across the whole domain at a given iteration and hence the effects anywhere in the domain is felt across the whole domain. This aids in faster convergence with respect to the number of iterations. Steady state solver was chosen for the current simulations. Density based solver in Fluent

solves the solution as shown in fig. 8. The density-based solver solves the governing equations of continuity, momentum, energy and species simultaneously. Governing equations for additional scalars like k & ϵ for $Std\ k-\epsilon$ model are solved sequentially [33]. Since they incorporate direct matrix inversion, implicit solvers require more memory for storage of the variables.

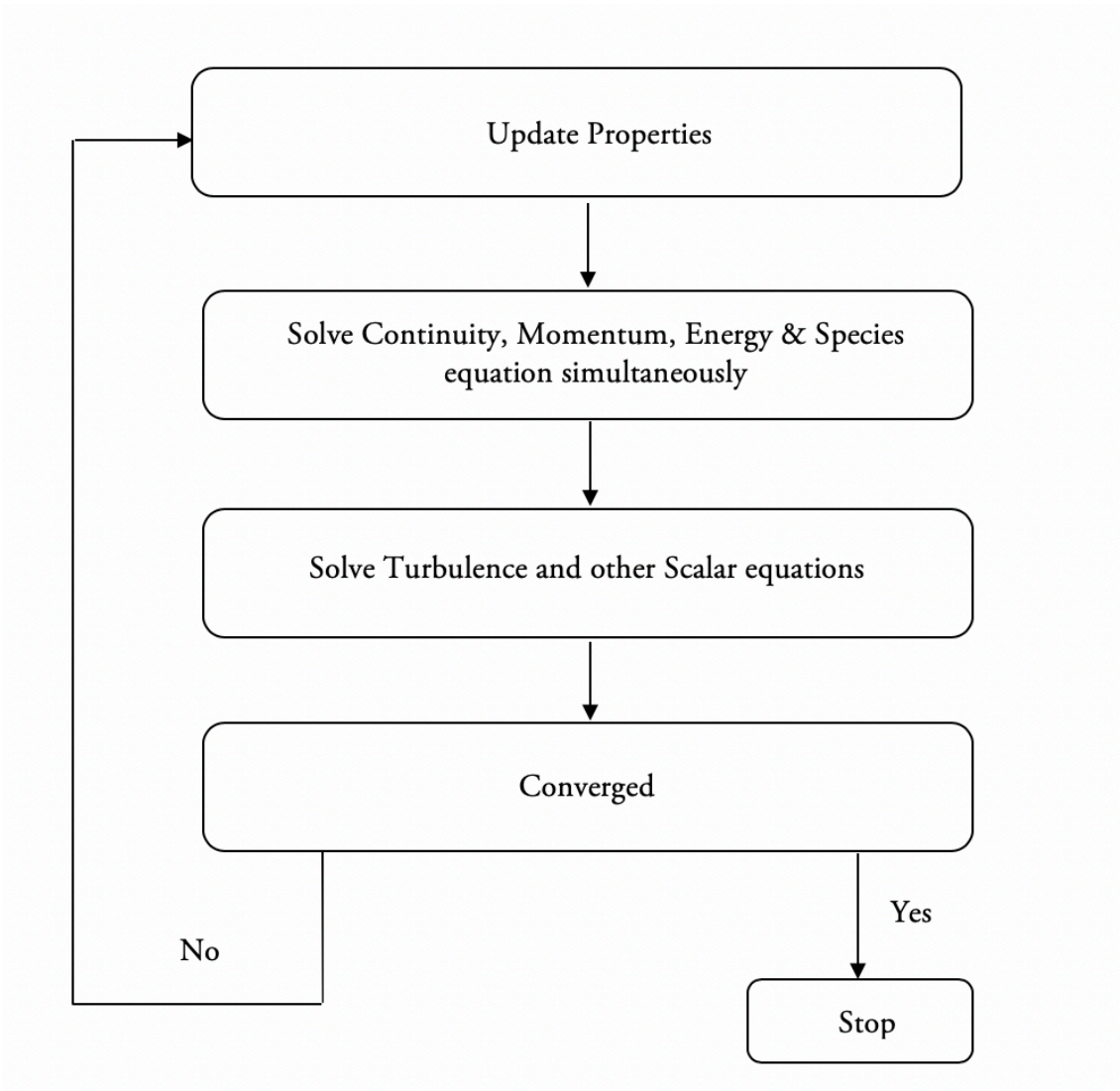

Figure 8. Density-based Solver [25]

4.4.2 Boundary Conditions

Boundary conditions used in the current CFD model is given in table 2.

Table 2. Boundary conditions for the current CFD model

Computation Boundaries	Boundary Condition	Value
Inlet	Pressure inlet	570168 *Pa,* 294 *K*
Hot exit	Pressure outlet	Varied to get different Cold Mass Fractions (ε)
Cold exit	Pressure outlet	101325 *Pa*
Walls	Adiabatic wall with no slip	Heat Flux = 0 W/m^2

*All pressure values are absolute values since the operating pressure was set to 0 Pa.

To achieve the different cold mass fractions used in the validation, the pressure at the hot exit was varied. Since this is a compressible flow problem and the flow variables are highly coupled, density based implicit solver was chosen with the ideal gas equation ($P = \rho RT$) used to model the pressure, temperature and density. The operating pressure was set to 0 Pa and hence all the pressure values were given as absolute values as this is the general convention followed during compressible flow simulations. Turbulent intensity and turbulent viscosity ratio were set at default values of 5% and 10 respectively at the inlet. Second order upwinding scheme was chosen for all the flow variables and all other under relaxation factors were left with default values.

4.4.3 Convergence Monitors

Convergence was monitored in two ways:

(1) All the residuals (continuity, momentum, energy, k & ϵ) were allowed to reach 1e-06.

(2) Total Temperatures at hot and cold exits were allowed to reach an asymptote.

(3) Mass weighted average total temperatures at the hot and cold exit were allowed to asymptote.

If issues were faced regarding convergence, then the courant number was reduced (usually from 5 to 1) and then the simulation was rerun.

4.5 Post-Processing

After the simulations converged, the fluent data file was exported to CFX-post which is a post processing software available in the ANSYS package. The state file with the information on the various planes and sections for the study of results was saved and then used with each data file. For graphs, the simulation values were exported to MS Excel and plotted. Python and journal scripting were also used during post processing whenever needed.

5. Validation

The initial validation was done with the Skye et al. [29] model. The above processes were repeated and the CFD runs were done.

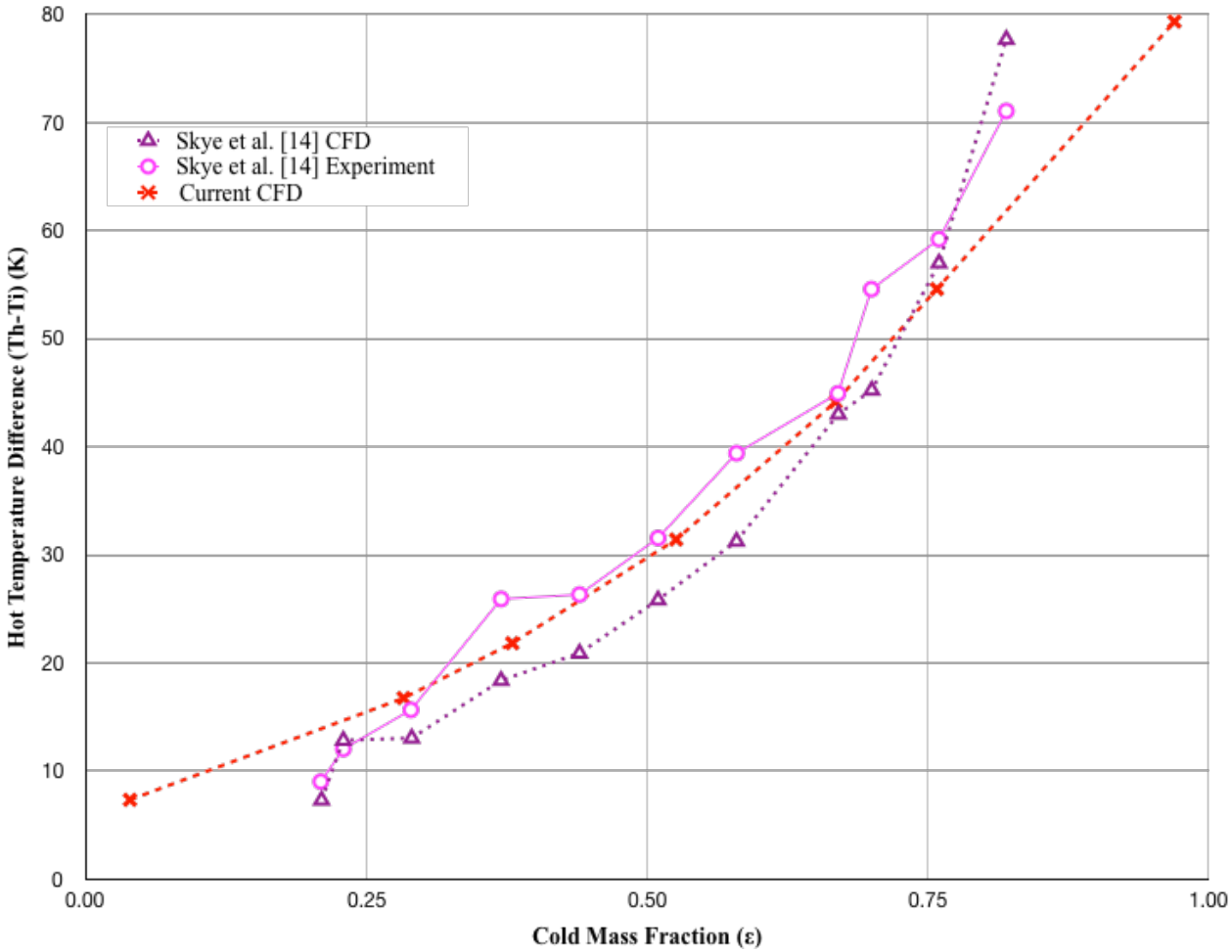

Figure 9. Hot temperature difference Vs Cold mass fraction

For the initial validation, a Polyhedral mesh was used. This is to save time as the validation is usually done to check the boundary conditions and the other parameters used. In Skye et al. work [29] the authors calculated the non-dimensional energy balance error and found this error to be more than

10% for cold mass fractions on both the extreme ends (high and low). Since the Cold mass fractions in the range of 0.18 - 0.82 had less than 5% error in the energy balance and were used to compare with the computational results.

From the fig. 9, it can be seen that the current CFD performs very well and has a pretty good match with the experimental curve in the case of the Hot exit temperature separation. The cold exit temperature separation shown in fig. 10 shows a slight overprediction in terms of the temperature difference but the current CFD has a much better match (difference less than 10%) than the one presented in the paper thus giving confidence in the simulations.

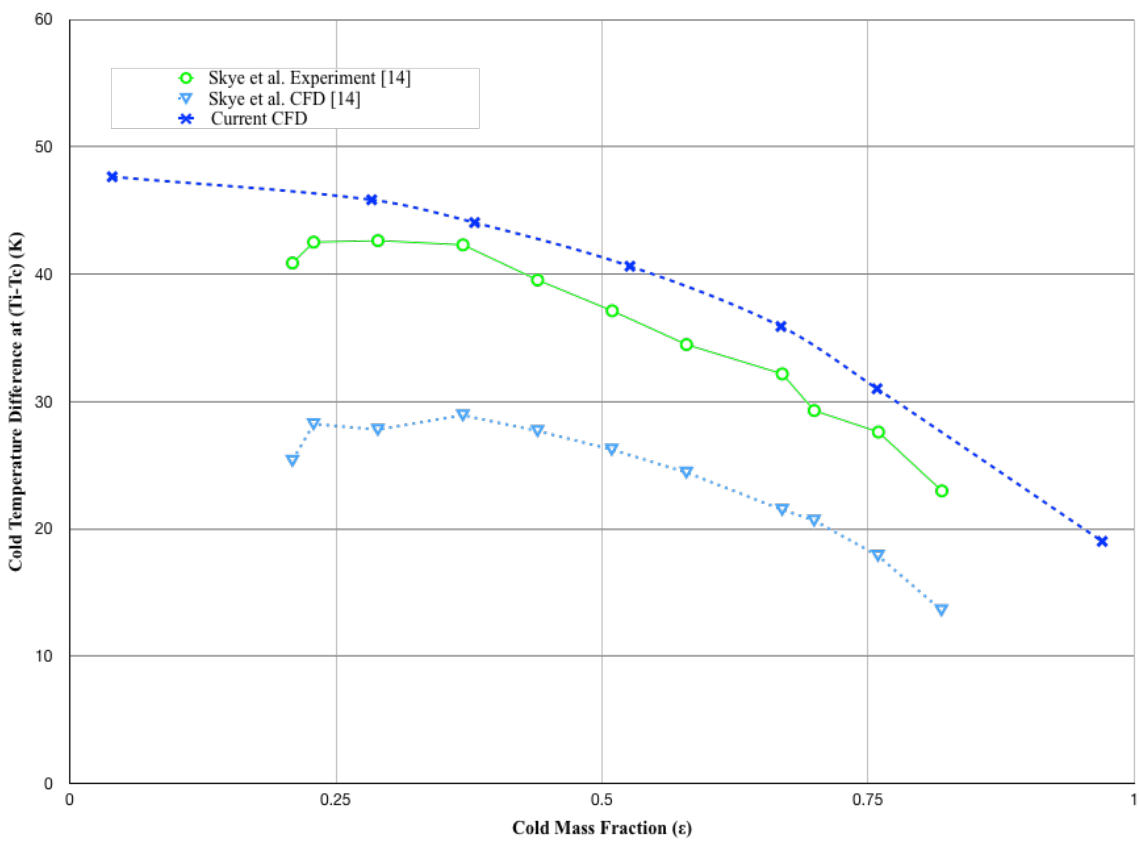

Figure 10. Cold temperature difference V s Cold mass fraction

6. Choice of Grid for Analysis

Once the validation of the model was done, the structured grid was chosen for further analysis. This is because of the following reasons:

(i) The structured grid although more difficult to generate initially provides more control and the grid can be modified in any region needed. Thus, making the grid finer in the regions where high gradients can be expected is easier with a structured grid.

(ii) The structured grid is also faster for the given number of cells when compared to its unstructured counterpart. This is because of the way in which the computational algorithm works.

(iii) A structured hexahedral mesh is more accurate than tetrahedral mesh for the same number of nodes [30].

7. Grid Sensitivity

Since the computational results depend on the grid domain and the number of elements in it. As the number of elements increases, the accuracy of the solution also increases. But care should be taken as to not over refine the mesh which might decrease the mesh quality in some areas and can cause some solution non-linearities to intensify which can cause the solution to not converge, as well as unnecessarily increase the computational costs.

Grid sensitivity was done with the structured grid. This was done in two ways. First, the total temperature at the hot and cold exits were monitored. Next, the Reynolds stress at the various sections in the Vortex tube were plotted for the various grids. The procedure for the calculation of the Reynolds Stress will be discussed in a later section. As it can be seen in fig. 11, the total temperatures asymptote at 3.26 million cells and shows no further change with an increase in the number of cells thus becoming grid insensitive at this point. The Reynolds stress Vs r plot in fig. 12 is shown for different axial locations along the length of the tube (x=20mm, 40mm, 60mm & 80mm). The background and the procedure for the calculation of the Reynolds Stresses are explained in a later section in this paper. From fig. 12, it can be seen that the curves for Reynolds Stress Vs Radius for different grids fall on top of one another. Note, for each of the visible curves in fig. 12, there are three curves that makeup that line showing all the three meshes produce the exact same results. This shows that the solution becomes grid independent at 3.26 million cells.

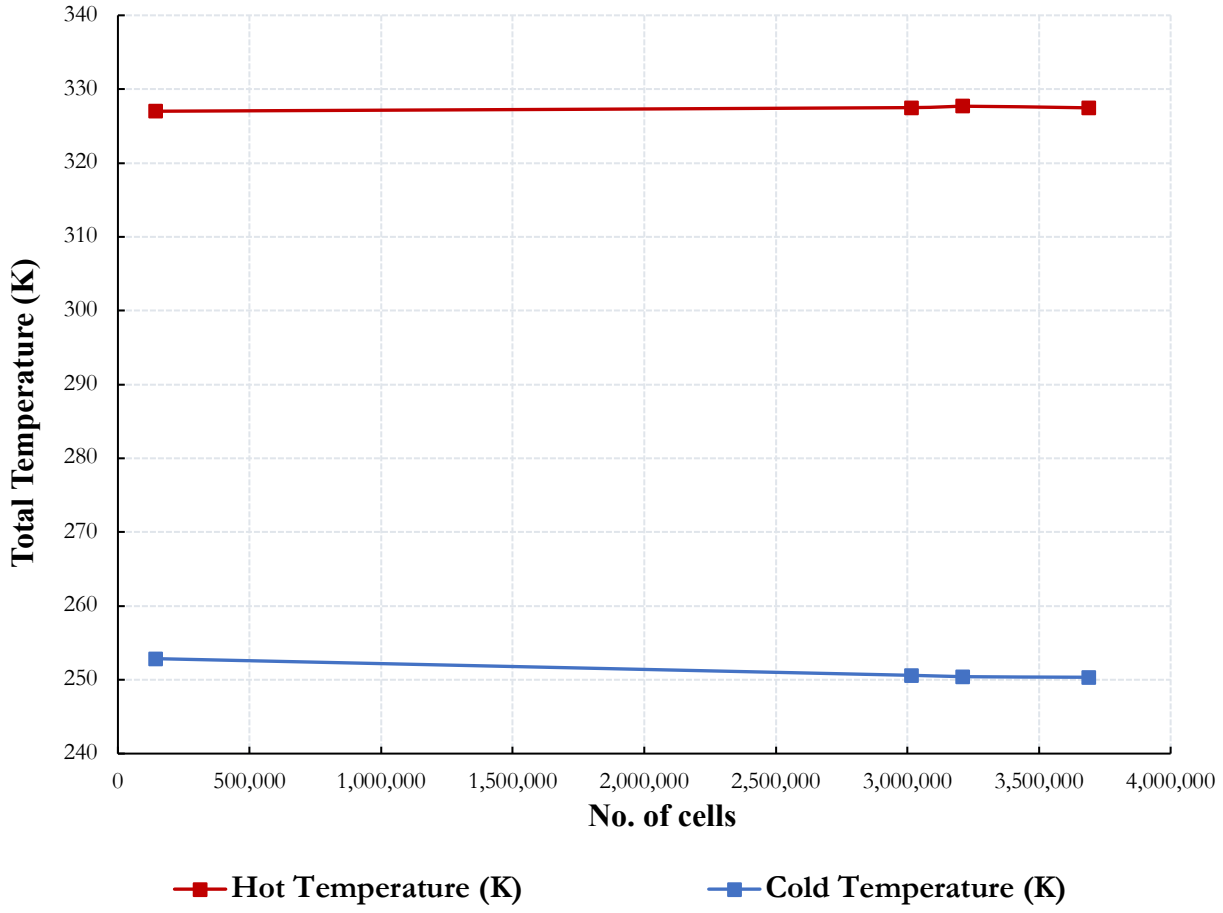

Figure 11. Grid sensitivity analysis

Grid Convergence Index (GCI) studies are some latest advancements to study the effectiveness of the grid refinement process whether the refined grid has reached the asymptotic limit i.e. has gotten closer to the exact solution. But since in the current study the parameters being monitored (Total Temperatures and the Reynolds Stresses) showed almost no change, the GCI was not of use and thus was not performed.

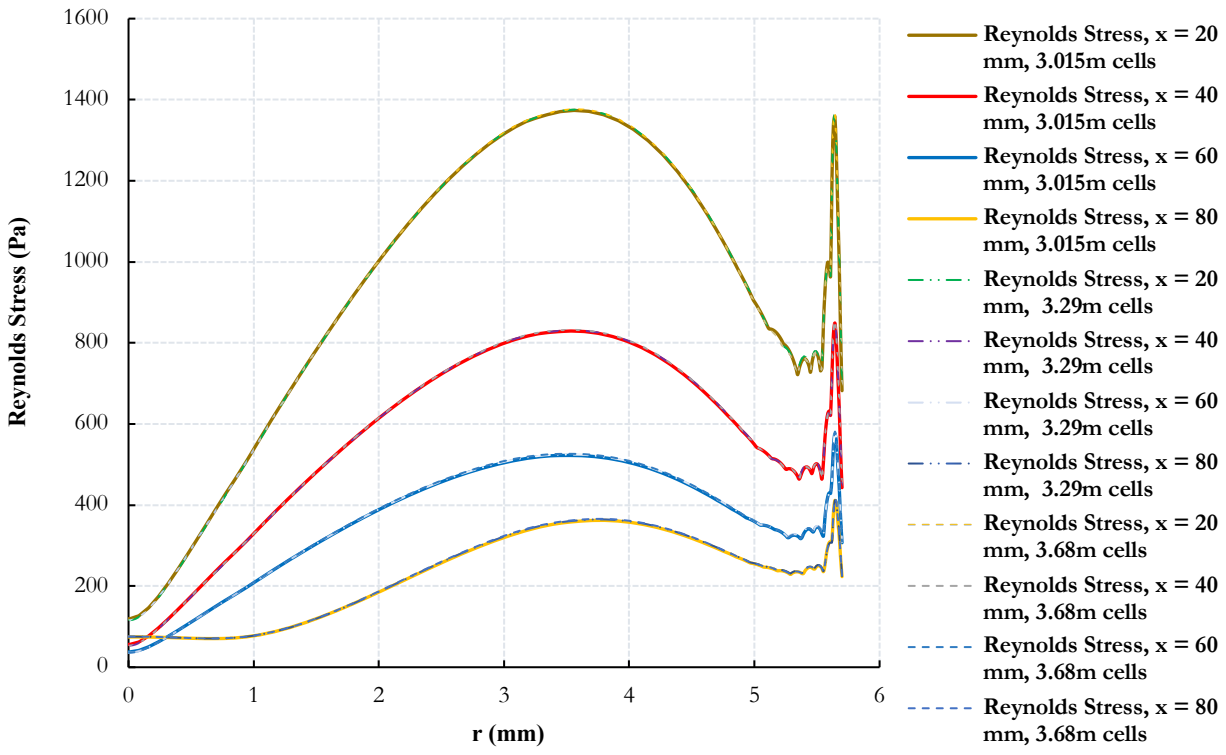

Figure 12. Reynolds stress at various axial locations for different grid sizes

Once the grid sensitivity was done, the grid with 3.29 million cells and the case with a Cold Mass Fraction (ε) of 0.526 was chosen for further analysis.

8. Analysis

Analysis was done in two steps:

(i) Initially the velocity and temperature profiles were compared to a LES computation from a published research to know where the RANS models perform similar and where they have their shortcomings.

(ii) The next step was to choose the parameters that were going to be studied and then analyzing them to come up with an explanation for the energy separation effect.

8.1 Comparison with LES research

8.1.1 Comparison of Tangential Velocity Profiles

The velocity magnitude and its components provide insight into the type of flow within the vortex tube. Since the flow within the confined vortex chamber is highly swirling, a Rankine vortex structure can be expected as suggested by previous research. In a Rankine vortex, the inner core of the flow has a forced vortex structure where the tangential velocity is proportional to the radius ($w \propto r$) and there is no relative motion between the fluid layers, this is also referred to as a region of solid body rotation. Beyond this radial location the flow transitions to a free vortex. After the transition region, there is the free vortex with tangential velocity inversely proportional to the radius ($w \propto \frac{1}{r}$). Generally, the free vortex region has a hyperbolic velocity profile with an equation $v \propto Cr^{-\alpha}$ where α varies from 0.71 to 0.78 [34].

Results of the current study computed with an inlet jet Re = 16,213 are presented at x = 36 mm and 56 mm and plotted in fig. 13 & 14. To provide a qualitative comparison the work of Secchiaroli et al. [20] is also presented. However, it must be noted that although they used a similar vortex tube, they had an inlet jet Re = 11,769, which is approximately 40% lower. The study used LES (Large Eddy Simulation), RSM (Reynolds Stress Model) and RNG $k - \varepsilon$ (Renormalization group) and reported the swirl, axial velocity, and static temperature profiles at different axial locations along the vortex tube. Due to the interference of the hot exit valve only two axial locations could be compared to our current study. These axial locations were equivalent to x=36 mm and x=56 mm in the present CFD simulations.

The normalized tangential velocity profiles are compared in fig. 13 & 14. Velocity normalization was performed by dividing the local velocity by the maximum velocity calculated by each model. Likewise, the normalized radius was determined by dividing the local radial position by the tube radius. From the figures, it can be seen that the tangential velocity computed by the $Std\ k - \epsilon$ model is qualitatively different from LES and RNG models. Using a +/- 5% as an indicator and estimating the various region the $Std\ k - \epsilon$ model predicts a forced vortex zone extending from the center to y/R of 0.7 and a transition zone up to y/R of 0.92 where the velocity stars to drop. The LES predicts a forced vortex region from the center to y/R of 0.26 and a transition zone up to y/R of 0.6 and then the velocity starts to drop as we move towards the annular region.

This result from the $Std\ k - \epsilon$ model is along expected lines as it has been shown in previous works [27,28] that the eddy viscosity models like $Std\ k - \epsilon$ which use a Boussinesq approximation for the Reynolds Stresses tend to neglect the anisotropic distribution of the normal stresses (u'^2, v'^2, w'^2) that arise in swirling flows. The eddy viscosity models also fail to take into account the

damping of the turbulent stresses due to swirl and this is turn causes them to predict an overly diffusive flow-field which reflects in the prediction of the tangential velocity profiles.

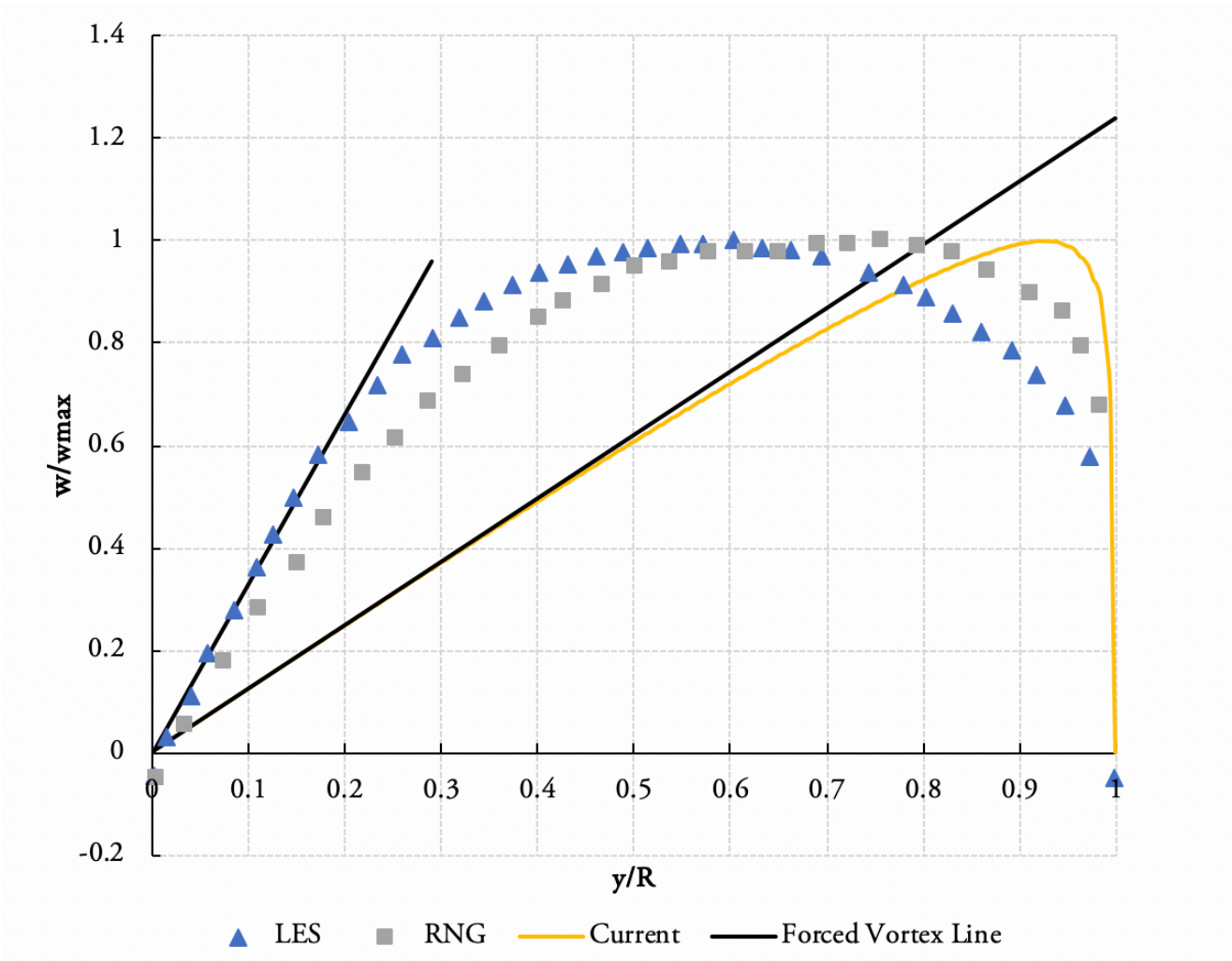

Figure 13. Normalized tangential velocity at x=36 mm

But in the case of the x=56 mm shown in Figure 8, $Std\ k-\epsilon$ produces similar results to the RNG $k-\epsilon$, but these are again very different from the ones given by the LES which predicts a hyperbolic velocity profile which corresponds to a free vortex flow all the way from y/R of 0.5 and a transition from forced vortex around y/R of 0.2. Since the RNG $k-\epsilon$ is a modification of the $Std\ k-\epsilon$ model

and is theoretically said to give improved results for rotating flows, strain dominated flows [14] because of the way in which the eddy viscosity is modelled to take into account the effects of swirl. The RNG $k-\epsilon$ thus produces a decent agreement with LES in the region closer to the inlet where the swirl intensity is higher and produces results similar to the $Std\ k-\epsilon$ at further axial distances as the swirl gets weaker.

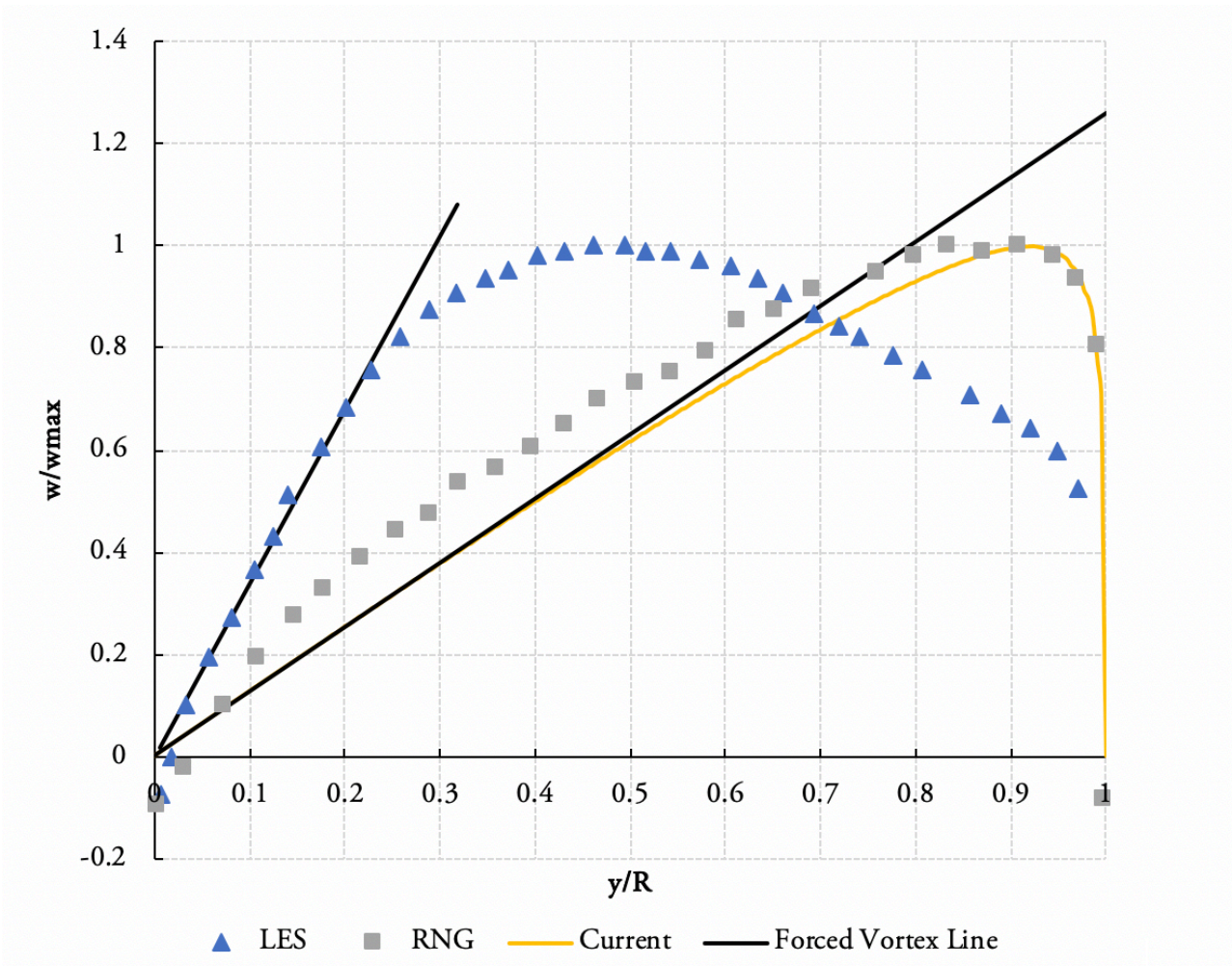

Figure 14. Normalized Tangential Velocity at x=56 mm

8.1.2 Comparison of Axial Velocity Profiles

Examining the Normalized Axial velocity profiles from fig. 15 & 16, the $Std\ k-\epsilon$ model appears to predict the cross-over point i.e. the region where axial velocity is zero, with a reasonable accuracy when compared with other models. $Std\ k-\epsilon$ model predicts an almost linearly increasing axial velocity profile from the cross-over point to the annular region whereas the LES and RNG predict a qualitatively different behavior. However, at the core the LES shows a region of flow oscillation in the forced vortex and the likelihood of a non-uniform flow in the core region. The RNG $k-\epsilon$ model which has a near one to one agreement in the free vortex region of the flow and is completely off in the forced vortex core and overpredicts the axial velocity by an extremely large margin below a y/R of 0.35. The $Std\ k-\epsilon$ on the other hand has a reasonable agreement with LES in the core region with the exception of the oscillation found in LES at y/R of around 0.3.

At x=56 mm, a similar trend can be observed. All the models agree well in terms of the cross-over region and show a similar behavior as the previous case above the cross-over region and towards the annular region. The cross-over region is the radial location where the axial velocity is zero and the flow above and below this region flow in the counter directions. This is an important zone as turbulence is expected to be produced here because of the shear between the two counter-flowing streams. Again, in the core region, the RNG $k-\epsilon$ tends to overpredict the axial velocity but the $Std\ k-\epsilon$ has a reasonable agreement with the LES model.

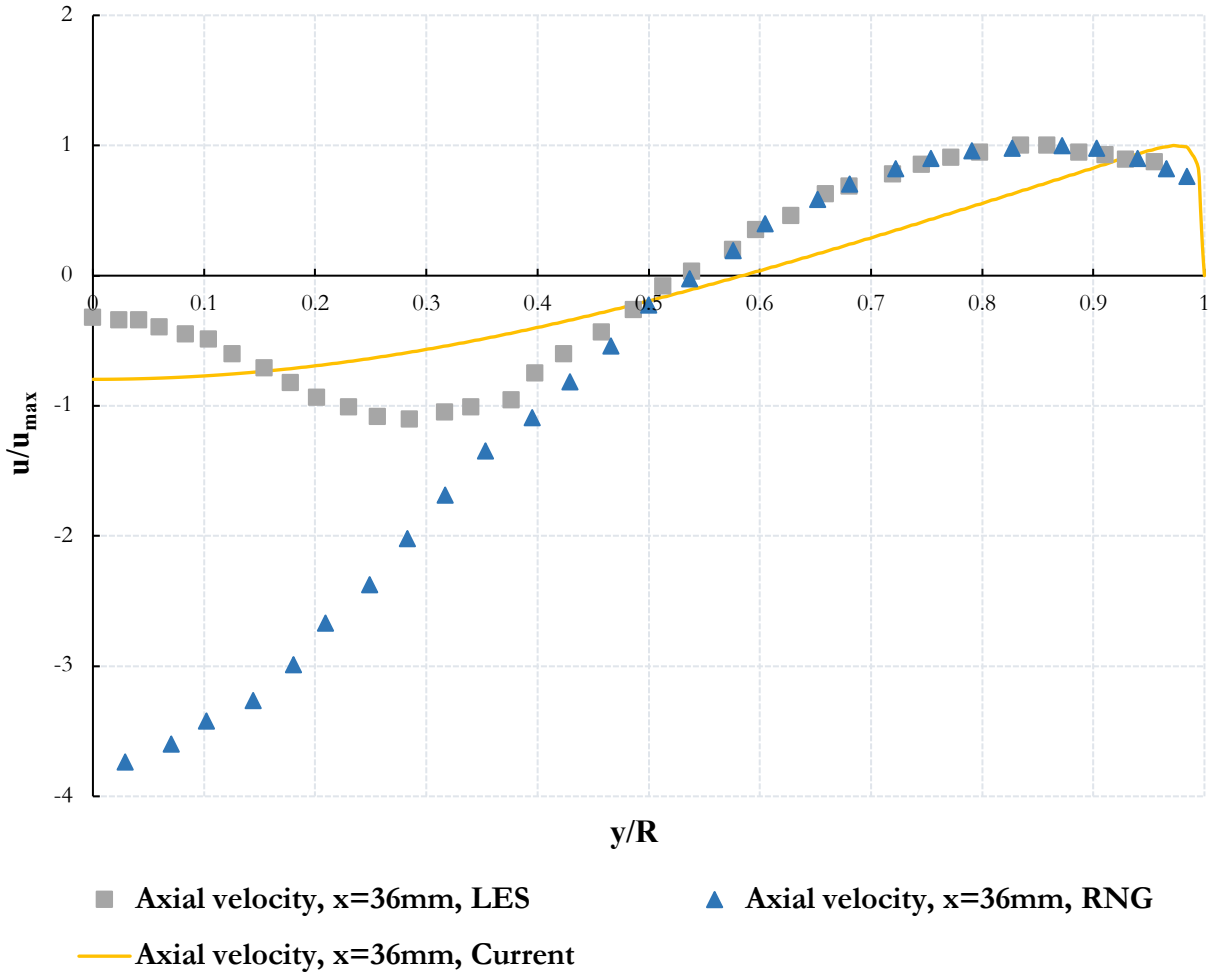

Figure 15. Normalized Axial Velocity at x=36 mm

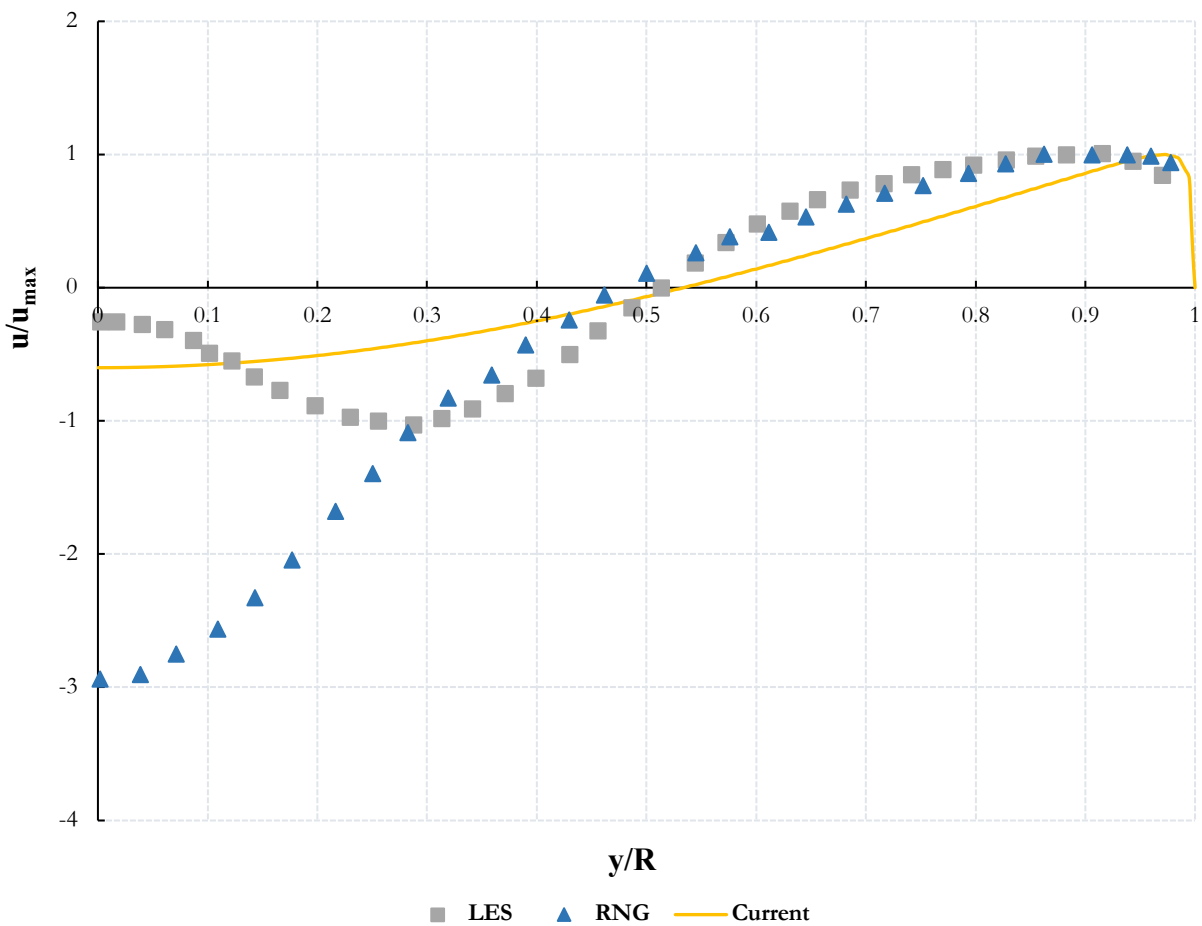

Figure 16. Normalized Axial Velocity at x=56 mm

8.1.3 Comparison of Static Temperature Profiles

The normalized static temperature profiles have also been compared in fig 17 & 18. Normalization was done by dividing the static temperature at each point by the maximum static temperature calculated at that plane by the model.

Static temperature curves are shown in fig. The $Std\ k-\varepsilon$ model shows an almost constant static temperature profile from the core all the way to a y/R of 0.9 and starts to increase at the wall. LES shows a drop-in temperature around y/R of 0.3 where the drop in axial velocity was observed and

shows an almost linear increase in temperature all the way to the wall. The RNG model again agrees well in the free vortex region and overpredicts the temperature drop in the forced vortex region below a y/R of 0.3. A possible reason might be the high axial velocities that the RNG model predicts in the core which tends to a lower pressure and ultimately lower temperatures.

A similar trend can be observed here but the maximum differences between the values have gone down to about 3.5%.

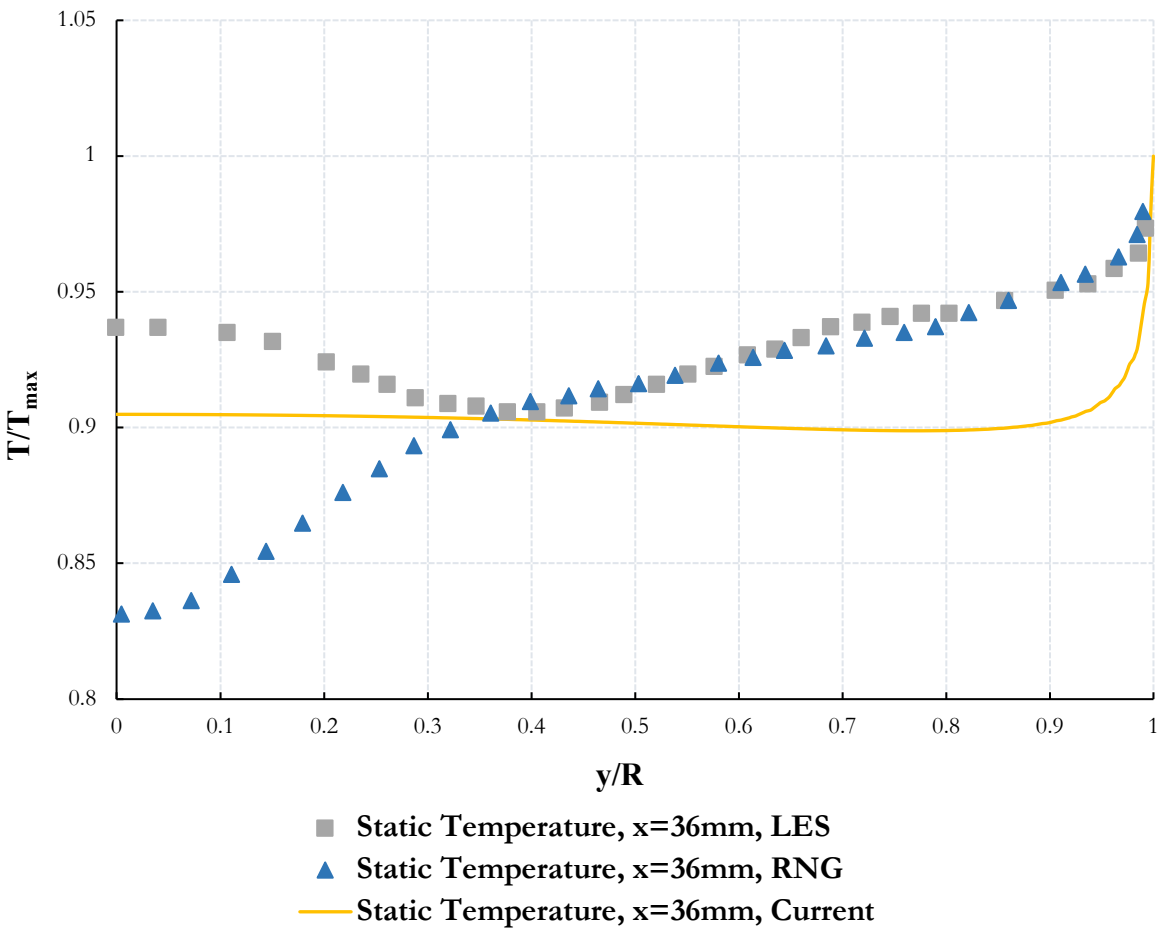

Figure 17.Normalized Static Temperature at x=36 mm

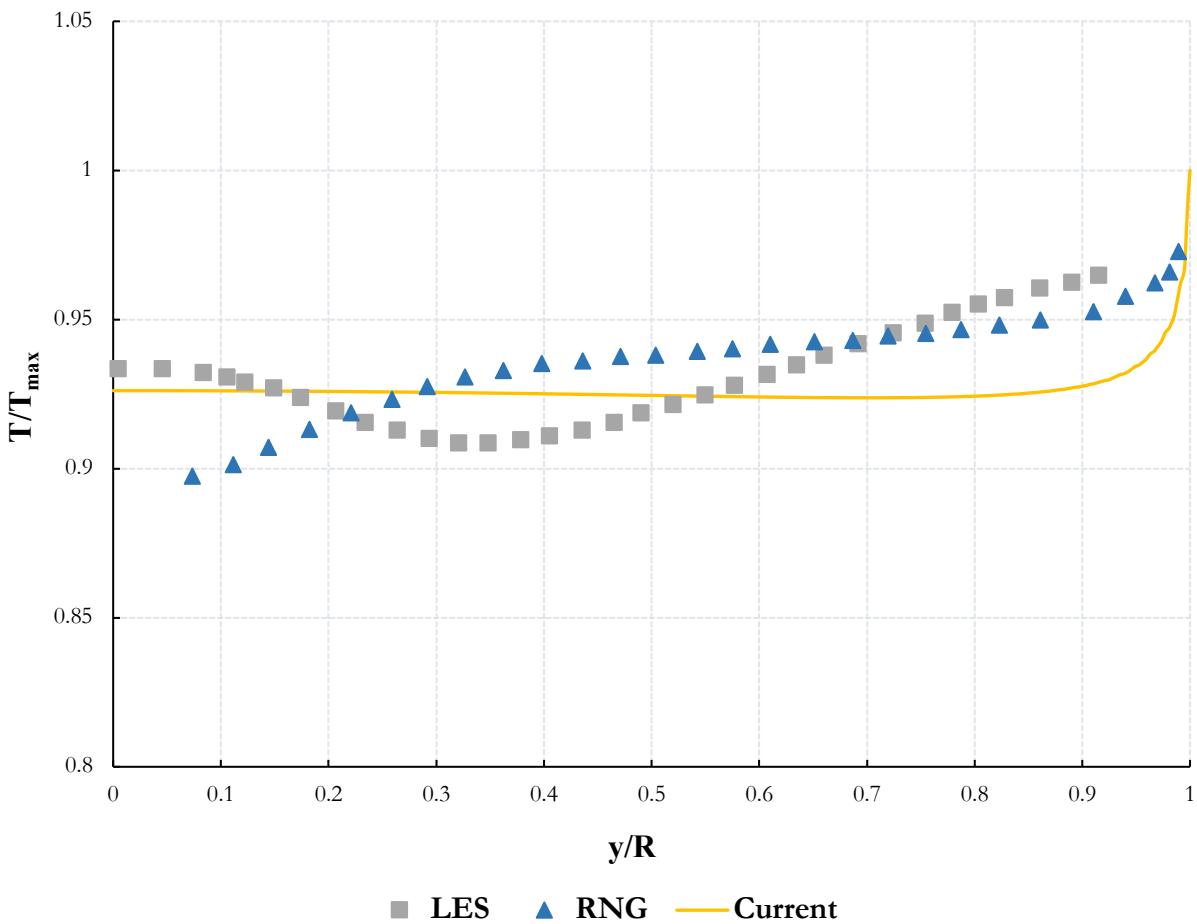

Figure 18. Normalized Static Temperature at x=56 mm

8.1.4 Observations

Having compared the three components of the flow i.e. the normalized tangential velocity, axial velocity and the static temperature profiles, the following observations have been made:

(i) The $Std\ k-\varepsilon$ model does not perform well when predicting the tangential velocity profile and the distribution of a Rankine vortex because of the way in which the eddy viscosity model which does not take into account the effects of swirl on the mean flow.

(ii) The axial velocity profiles on the other hand are predicted fairly good by the $Std\ k-\varepsilon$ model with the exception of the non-linearity observed in LES in the core region.

(iii) The Static Temperature profile predicted by $Std\ k-\varepsilon$ is almost flat in the central regions of the tube and shows an increase in the region near the tube wall.

With an idea of the various benefits and the shortcomings of the $Std\ k-\varepsilon$ model, we will go on to the analysis of the flow and the mechanism responsible for the energy separation.

8.2 Analysis of Flow Properties

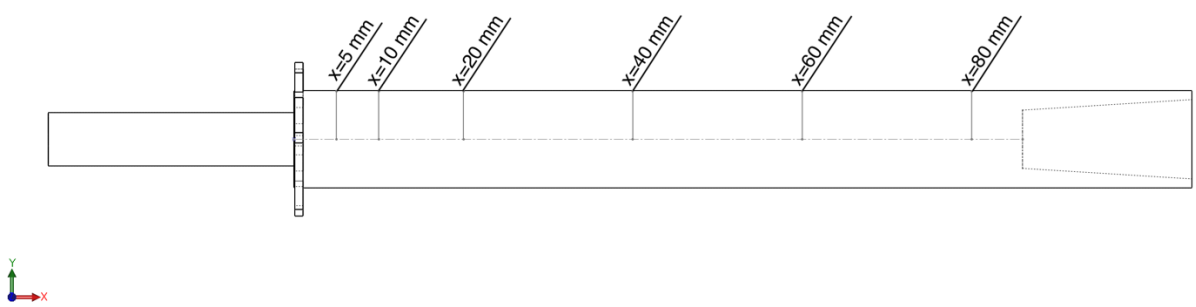

Figure 19. The stations at which the results are studied

The current vortex tube simulations and the corresponding analysis of the results have all been performed in the Cartesian Coordinate system and the results are converted to a cylindrical coordinate system when needed. The origin (x, y, z = 000) is located along the vortex tube center line and at the plane of junction between the vortex tube main cylinder (right hand side of the origin) and the cold exit tube (left hand side of the origin). The orientation of the vortex tube with respect to the coordinate system and the location of the origin can be seen in fig. 19.

Since the flow within the vortex tube is highly three-dimensional, all the three components of velocity i.e. the tangential, radial and the axial components within the vortex tube main cylinder were examined. This section is also referred as Hot section. In the current study radial lines represent the downstream locations where the computational results are presented. These locations are x = 5mm, 10 mm, 20 mm, 40 mm, 60 mm and 80 mm. Beyond the 80 mm downstream from the nozzle inlet is the hot exit control valve surface, which begins to interfere with the flow therefore no axial locations beyond the 80 mm considered in the current study.

Note:

From here on, all the results presented correspond to the simulation at $\varepsilon = 0.526$. The conditions for this case are Inlet Pressure = 570,168 bar, Hot exit pressure = 210,000 bar, Cold exit pressure = 101,325 bar.

8.2.1 Velocity Analysis

The flow has three velocity components namely (i) Axial Velocity (Velocity u), (ii) Radial velocity (Velocity v) and (iii) Tangential velocity (Velocity w). The primary component of the velocity in swirling flows is the tangential velocity. As seen before, the flow can be divided into three different regions along the radius using the tangential velocity profile. The central region is the forced vortex region, also referred to as the region of solid body rotation because here the tangential velocity is linearly proportional to the radius. The outer region where the tangential velocity varies hyperbolically with respect to the radius is called as the free vortex region. The transition region resides between the forced and free vortex regions.

Fig. 20 shows the tangential velocity distribution from the current simulation. As seen in the above comparisons, the velocity profiles show an increasing magnitude towards the wall. The velocity starts to drop at a radial location of approximately 5.35 mm (except at x=5 mm) signaling a start of transition region which eventually turns into the free vortex region and reaches zero speed at the wall because of the no slip condition imposed by the wall boundary condition.

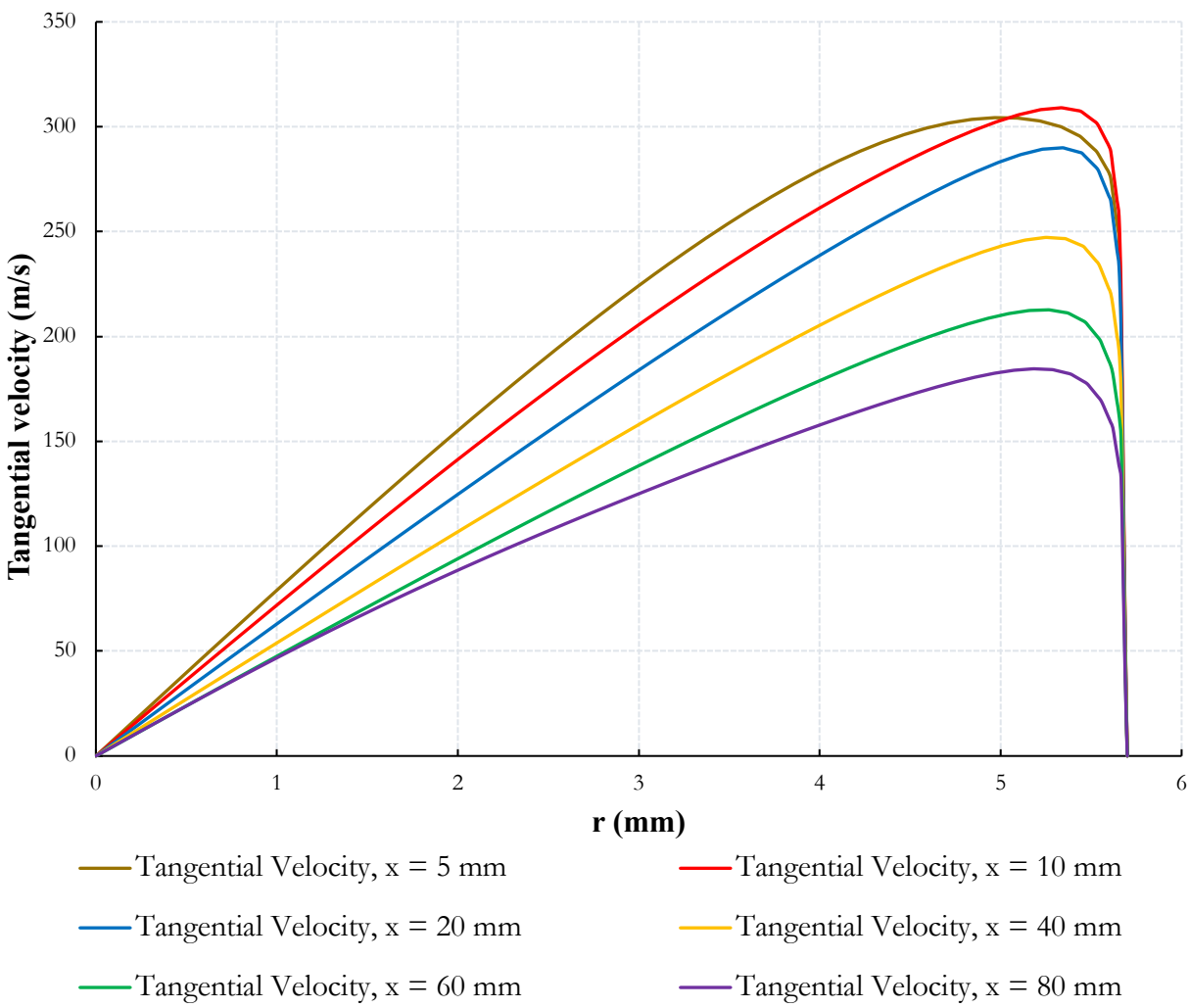

Figure 20. Tangential velocity distribution at various axial locations

The second major component is the Axial velocity or Velocity u component shown in fig. 21. In the current model, the orientation of the vortex tube with respect to the coordinate system makes the part of flow with a positive axial velocity as the one flowing towards the hot exit and vice versa. The radial location where the axial velocity goes to zero and changes sign is called as the cross-over region. This location is used to differentiate the cold and hot flows. This is also the region apart from the near wall where high shear stresses can be expected. As the two counter flowing streams cross each other, they produce shear and the shear in turn generates turbulence which can be confirmed by looking at the Reynolds stresses. The Reynolds stress forms the turbulence production term in the momentum equations.

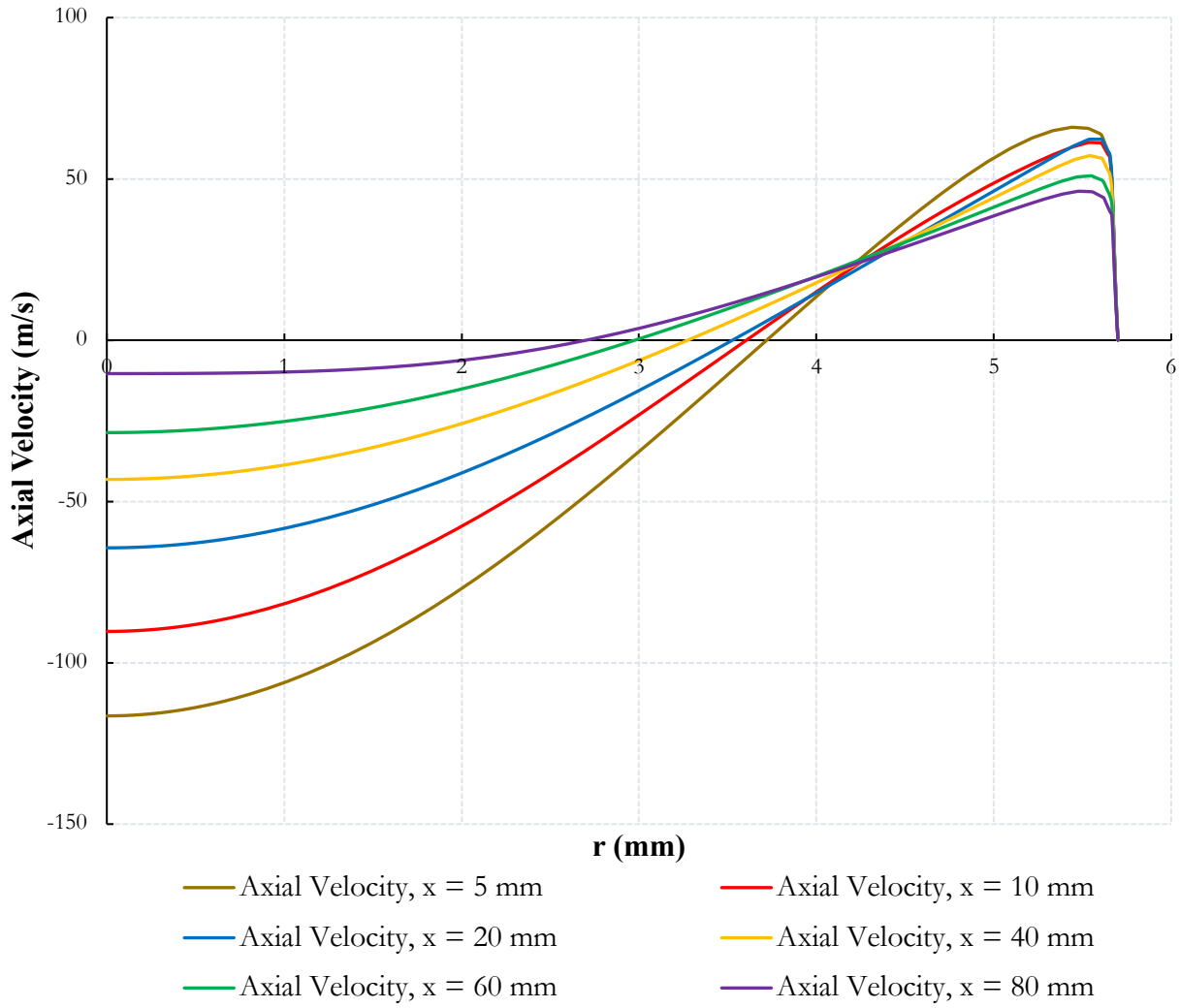

Figure 21. Axial velocity distribution at various axial locations

It can also be seen that the radial location of the flow reversal decreases as we move towards the hot end in fig. 22. If all the cold flow has reversed at a particular axial location axial velocity at the centerline would be zero axial and no negative axial velocities would be found beyond this point, and this would be called the stagnation point. Previous vortex tube studies have shown that the maximum total temperature of the annular flow can be observed at the axial location where this stagnation point is located and that the total temperature does not increase further beyond this region. However, presence

of such a stagnation point was not observed in the current study due to the geometry and conditions used for the vortex tube.

Fig. 20 shows the location of the zero axial velocity i.e. the interface between the two flows at various axial locations along the tube. From this it can be seen that the flow reversal region keeps shrinking as we move towards the hot exit. The movement of the interface location towards the centerline shows a linear trend (shown in the R^2 value for linear fit) as we move downstream from the inlet.

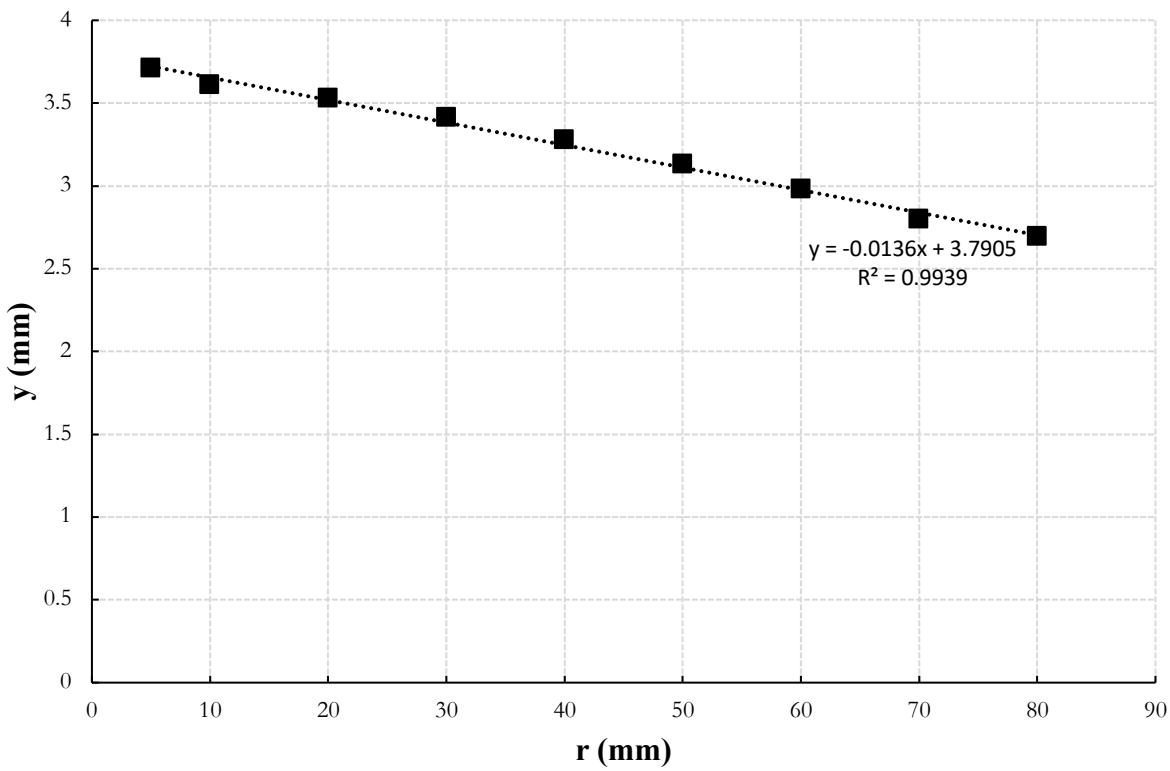

Figure 22. Cross-over locations at various Axial locations

8.2.2 Vorticity and Strain rate

The two important parameters that have to be studied in order to understand the flow better are Vorticity and the Strain Rate. If we imagine a fluid packet to be a cube present in the fluid flow and the flow to be a collection of such fluid packets, then these are the two effects that the fluid packet undergoes in a flow and together they make up the deformation tensor. Vorticity is the rate at which the fluid packet i.e. the cube rotates, and the strain rate is the rate at which the fluid packet undergoes deformation in the form of shear.

$\frac{\partial U_i}{\partial x_j}$ - Deformation tensor

$$\frac{\partial U_i}{\partial x_j} = \frac{1}{2}\left(\frac{\partial U_i}{\partial x_j} + \frac{\partial U_j}{\partial x_i}\right) + \frac{1}{2}\left(\frac{\partial U_i}{\partial x_j} - \frac{\partial U_j}{\partial x_i}\right) \tag{9}$$

where, $S_{ij} = \frac{1}{2}\left(\frac{\partial U_i}{\partial x_j} + \frac{\partial U_j}{\partial x_i}\right)$ - Symmetric part (or) Strain rate

$\omega_{ij} = \frac{1}{2}\left(\frac{\partial U_i}{\partial x_j} - \frac{\partial U_j}{\partial x_i}\right)$ - Skew-symmetric part (or) Vorticity

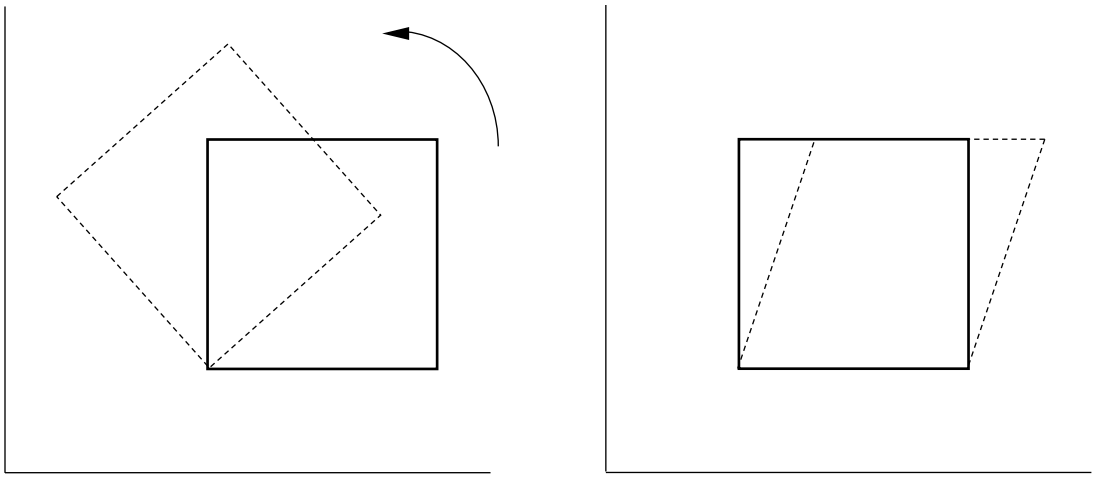

Figure 23. Vorticity (left), Strain (right)

A constant vorticity with no shear should be expected in the forced vortex region. In the free vortex region, the vorticity should go towards zero as the free vortex flow is irrotational. The fig. 23 shows the Axial Vorticity (Vorticity X in current simulation) in various axial locations downstream of the nozzle inlet. The vorticity changes considerably in the axial locations at 5 mm and 10 mm with the forced vortex region being very small. Further downstream, at other axial locations (20, 40 & 60 mm), the vorticity remains fairly constant in the central regions with the gradient being small in the forced vortex region and then dropping to a zero magnitude in the annular region, only to increase because of the boundary layer effects close to the wall. Again, at x = 80 mm, the vorticity curve shows considerable change even close to the center and this can be attributed to the presence of the hot valve which causes disturbances to the flow as this axial location lies very close to the hot valve.

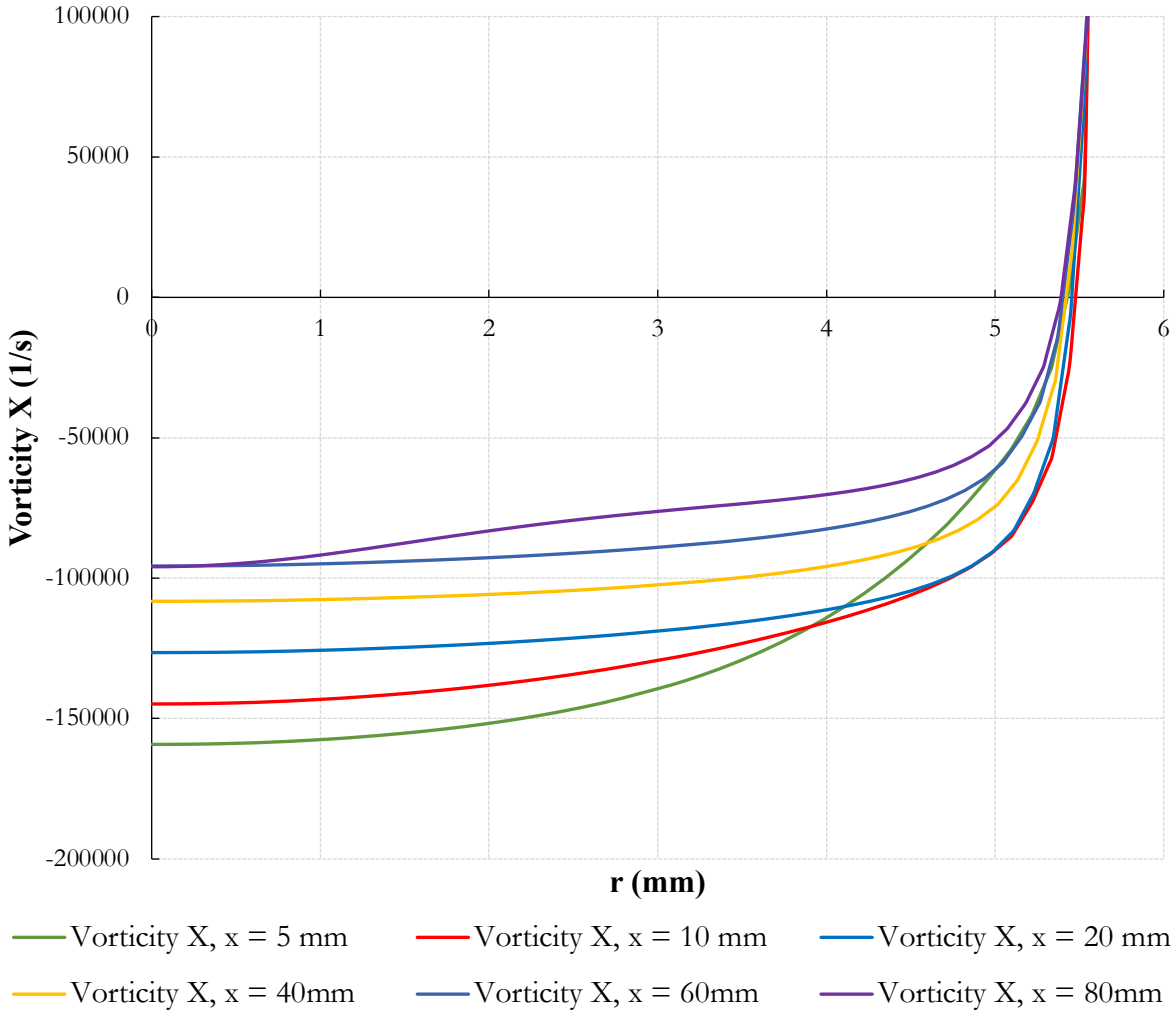

Figure 24. Axial vorticity or Vorticity X at various axial locations

The vorticity changes by approximately 9% from the tube centerline to the location where the axial velocity goes to zero at a stream wise i.e. axial location of x=20 mm. Since we know that the core flow is a forced vortex flow, we have fixed the condition that any change in vorticity less than 10% will be considered as approximately constant and thus represent the forced vortex zone. This agrees with other locations as well (x=40 & 60 mm).

Strain rate reported here is directly output from ANSYS Fluent which defines strain rate as the second invariant of the deviatoric stress tensor. Hence, strain rate is the rate of shear deformation the fluid packet undergoes. Strain rate plot is shown in fig. 25 and it can be observed that the strain rate is very low in the core flow which is the forced vortex flow. It then increases and has an inflection point at around radius of 3 mm if we look at the x=10-, 20- and 40-mm curves where the gradient of the rise drops. It then has another inflection point at radius of 5 mm from where it starts increasing exponentially towards the annular region reaching very high values near the wall.

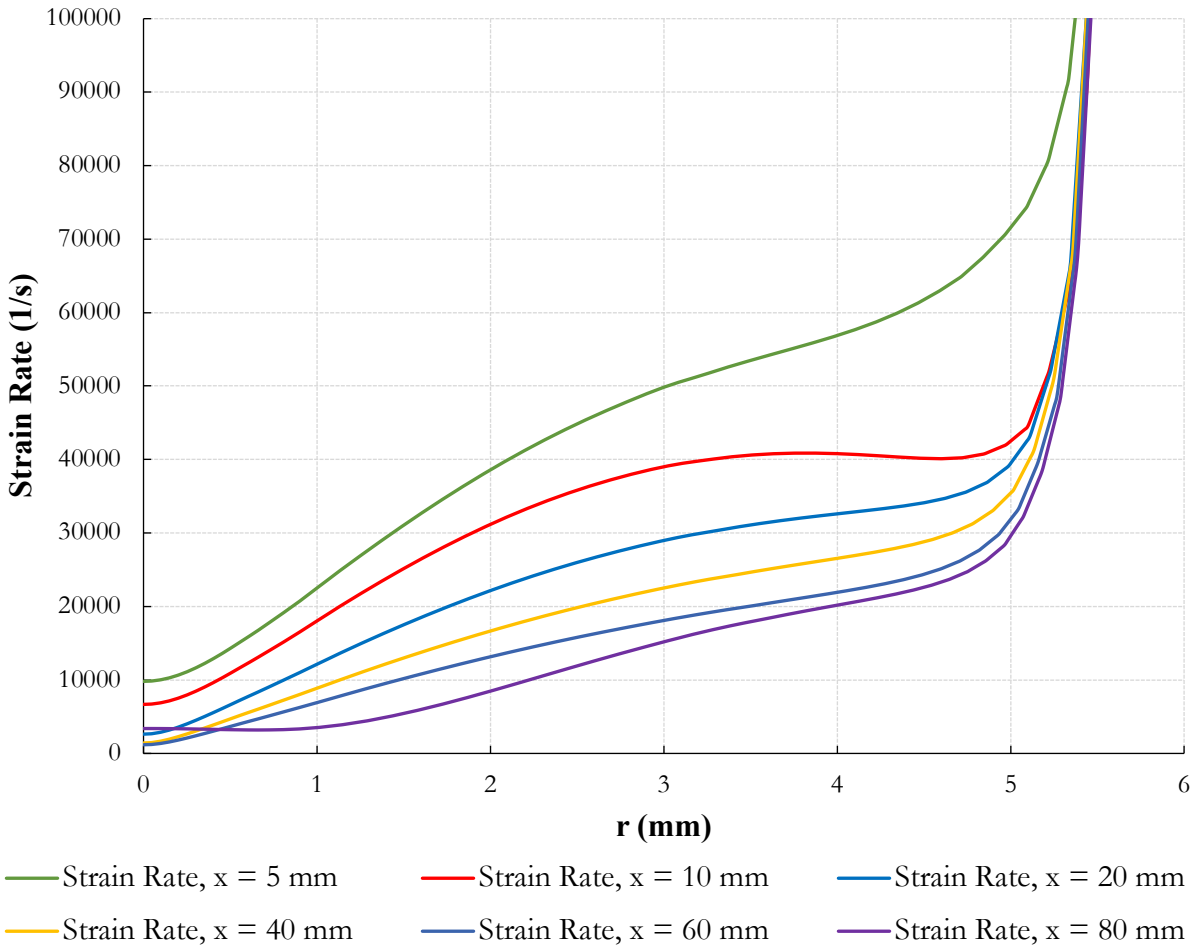

Figure 25. Strain rate at various axial locations

8.2.3 Reynolds Stress

Consider a flow shown in figure where the average flow velocity is a function of y i.e. $U = U(y)$. The instantaneous velocity of a flow field is given by,

$$u = U + u' \tag{10}$$

Where U is the average velocity and u' is the turbulent macroscopic fluctuating velocity. The microscopic flow i.e. the flow at the molecular level is given by a similar equation but the u' is replaced with u'' which is the fluctuating velocity at the molecular level. Consider a momentum flux traveling from a point P in the flow field to a point Q. The instantaneous flux is given by,

$$dp_{xy} = \rho(U + u'')v''dS \tag{11}$$

Here as per the tensorial notation, dP_{xy} denotes a flux directed perpendicular to x-axis in the direction of y-axis in the 3D plane. If we perform an ensemble average on the equation, we get

$$dP_{xy} = \overline{\rho u'' v''}dS \tag{12}$$

$$\tau_{xy} = -\overline{\rho u'' v''} \tag{13}$$

Using kinetic theory of gases and some manipulations [37], the shear stress can be approximated as,

$$\tau_{xy} = \mu \frac{dU}{dy} \tag{14}$$

Where μ, the molecular viscosity is given by,

$$\mu = \frac{1}{2}\rho v_{th} l_{mfp} \tag{15}$$

Where v_{th} - thermal velocity of the molecules

l_{mfp} - length of mean free path of molecules i.e. the distance traveled by a molecule before colliding with another molecule.

Prandtl then came up with the mixing length hypothesis for a turbulent motion wherein he pictured turbulence as a lump of fluid particles clinging together and moving as a whole. He replaced the thermal velocity (v_{th}) by mixing velocity (v_{mix}) and the length of mean free path (l_{mfp}) by mixing length (l_{mix}). The mixing length is the distance the lump travels while it retains its momentum.

Hence, the shear stress generated due to turbulent motion is given by,

$$\tau_{xy} = \frac{1}{2}\rho v_{mix} l_{mix} \frac{dU}{dy} \tag{16}$$

Where,

$$\mu_t = \frac{1}{2}\rho v_{mix} l_{mix} \tag{17}$$

is the turbulent viscosity. Thus,

$$\tau_{xy} = \mu_t \frac{dU}{dy} \tag{18}$$

In general, the Reynolds stress is given in tensorial form as,

$$-\overline{u_i' u_j'} = \mu_t \left(\frac{\partial \overline{u_i}}{\partial x_j} + \frac{\partial \overline{u_j}}{\partial x_i} \right) - \frac{2}{3} k \delta_{ij} \tag{19}$$

If we look closely into the eq. 16, Reynolds stresses are treated like viscous stresses and are equated to the velocity gradient by introducing eddy viscosity. Eddy viscosity (μ_t) (also called as turbulent viscosity) performs role similar to molecular viscosity but it is a property of the flow rather than the fluid. Hence, has to be modeled through appropriate equation (refer eqn. (5)).

Reynolds Stress is calculated here from the eq. 20, where both the quantities eddy viscosity and strain rate are reported directly by fluent.

Reynolds Stress = Eddy Viscosity (μ_t) x Strain rate (20)

The turbulence models differ in the way they treat the eddy viscosity with the Prandtl's mixing length model being the most basic and there are more advanced models specifically developed for certain flows. The $Std\ k - \epsilon$ model used in the current analysis is a two-equation isotropic eddy viscosity model which solves a turbulence kinetic energy and dissipation term to calculate the eddy viscosity. One of the drawbacks of the isotropic eddy viscosity models like the $Std\ k - \epsilon$ can be seen here. The eddy viscosity shown in fig. 26 is calculated to be almost uniform from the center to the annular region

with the eddy viscosity dropping to zero near the wall. Whereas eddy viscosity should be expected to be low at the core because of the ability of forced vortex to be resistant to the turbulent momentum transfer, then peaking at the region where axial velocity goes to zero because of shear between the two counter-flowing streams and again dropping to zero near the wall [38].

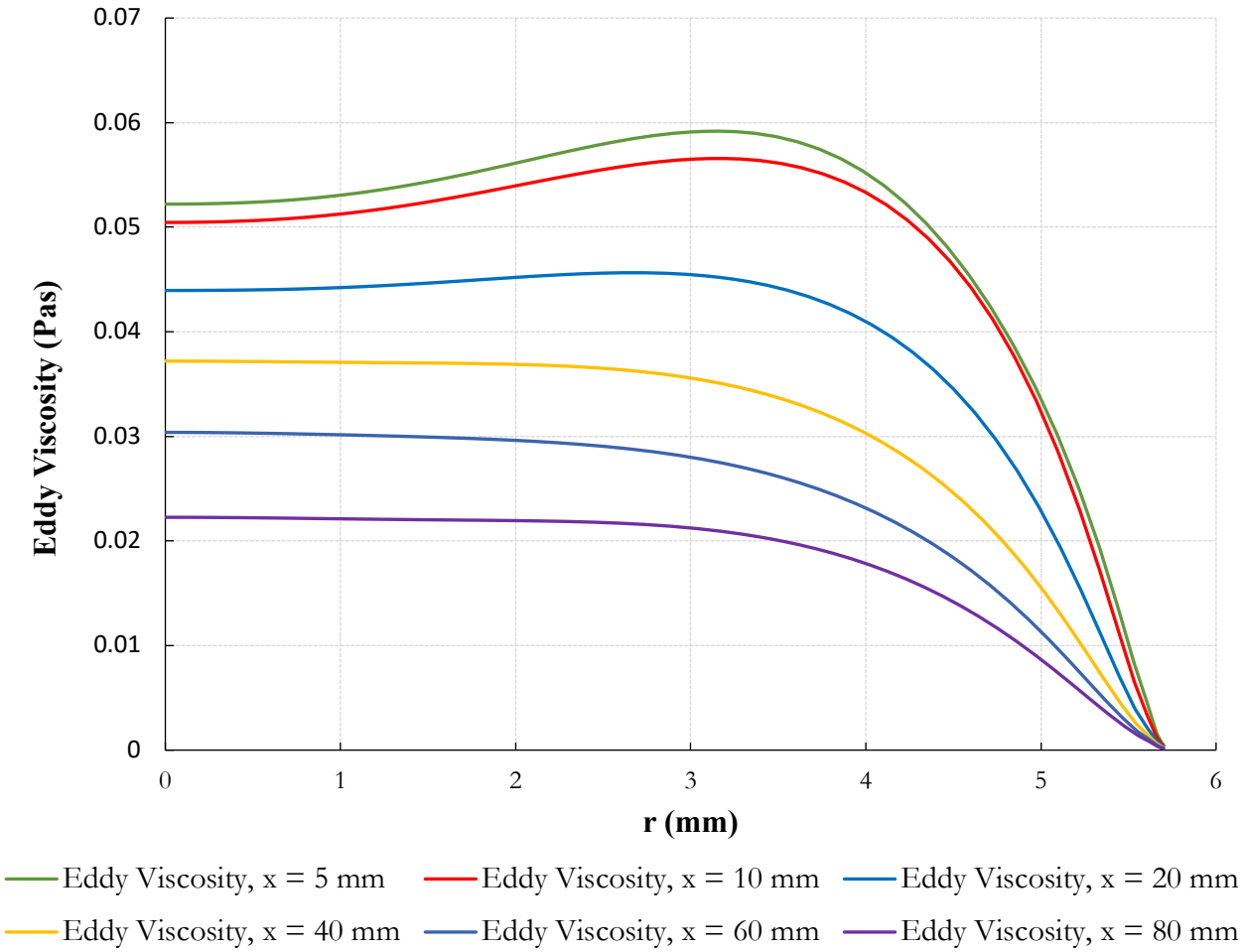

Figure 26. Eddy viscosity at various axial locations

From the fig. 27, we can observe that the Reynolds stress is very low in the core flow and increases with radius and peaking around the center of the radial location. It then starts dropping towards the annular region and has a sudden peak near the wall before dropping to zero at the wall. The overly diffusive profile of the eddy viscosity has resulted in a similar characteristic for the Reynolds Stress.

The Reynolds Stress although predicted to be high in the region of the zero-axial velocity can be seen to have a bigger spread than what is normally expected [36].

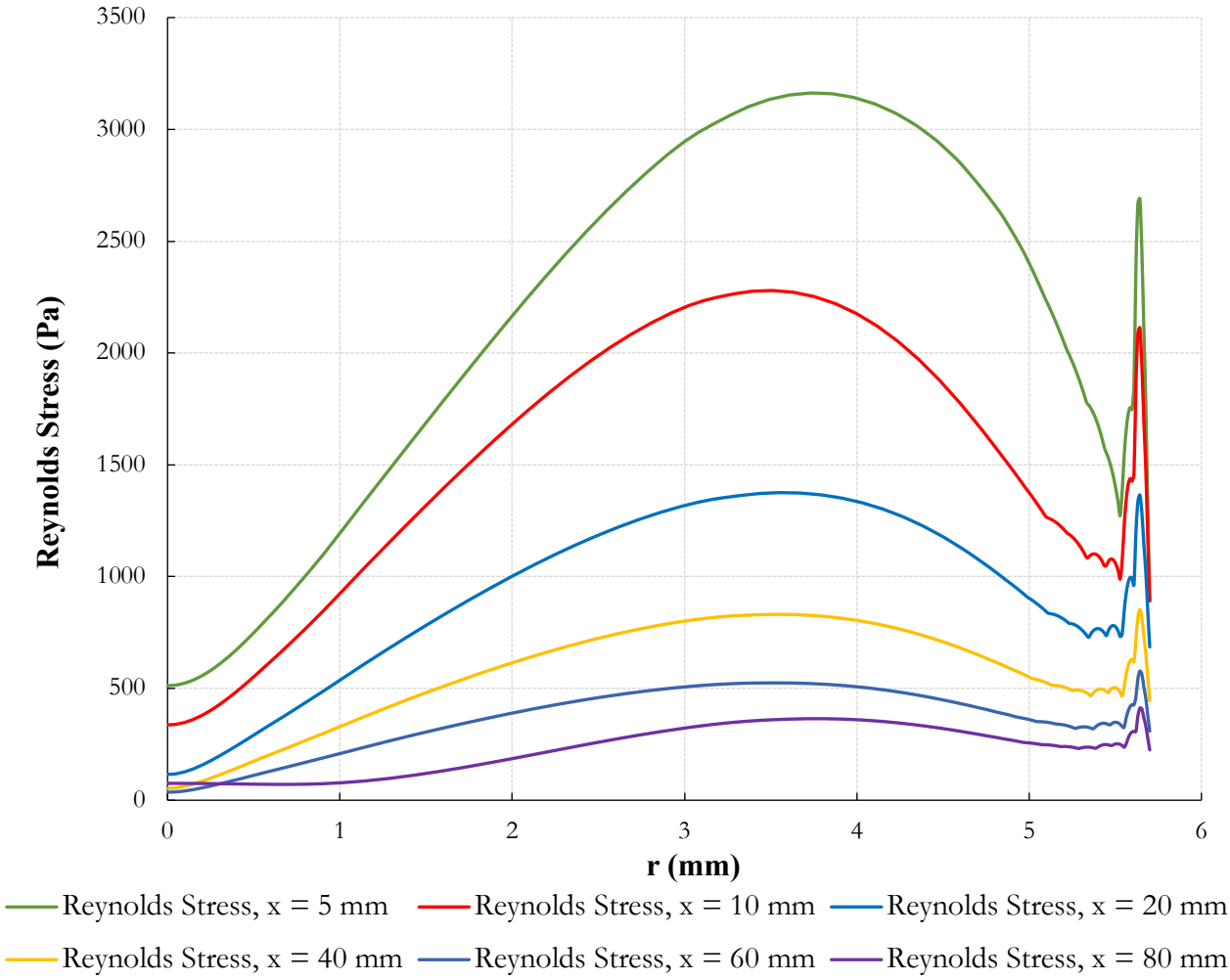

Figure 27. Reynolds Stress at various axial sections

Reynolds stress describes the production of shear due to turbulence. In highly swirling flows, the Reynolds stress displays an anisotropic effect i.e. the stresses are different along the different planes. But in the current simulation we have used an isotropic eddy viscosity turbulence model (Std $k - \epsilon$) which does not take into account any anisotropic effects [36]. Thus, we get a single Reynolds stress value at each location which provides the overall average shear at a given location. From fig. 9, we can

observe that the Reynolds stress peaks at the radial location where the axial velocity cross over occurs (which is denoted by the vertical arrows within the plots). This is also consistent with every axial location except at x=80mm where the flow gets affected by the presence of the hot valve and thus the location of the maximum shear also shifts. But overall, this result aligns with our expectation that the shear produced at the interface between the two counter-flowing fluid streams must have the highest Reynolds stress, and that this is the cross-over region. The forced vortex has a tendency to suppress turbulent momentum transfer whereas a free vortex permits the transfer of momentum between the flow layers [39]. The turbulence produced due to this shear must breakdown and this occurs in the free vortex region that allows turbulent momentum transfer. This turbulence finally breaks down giving rise to viscous dissipation near the wall. Dissipation gives rise to the increased temperature found in the annular region.

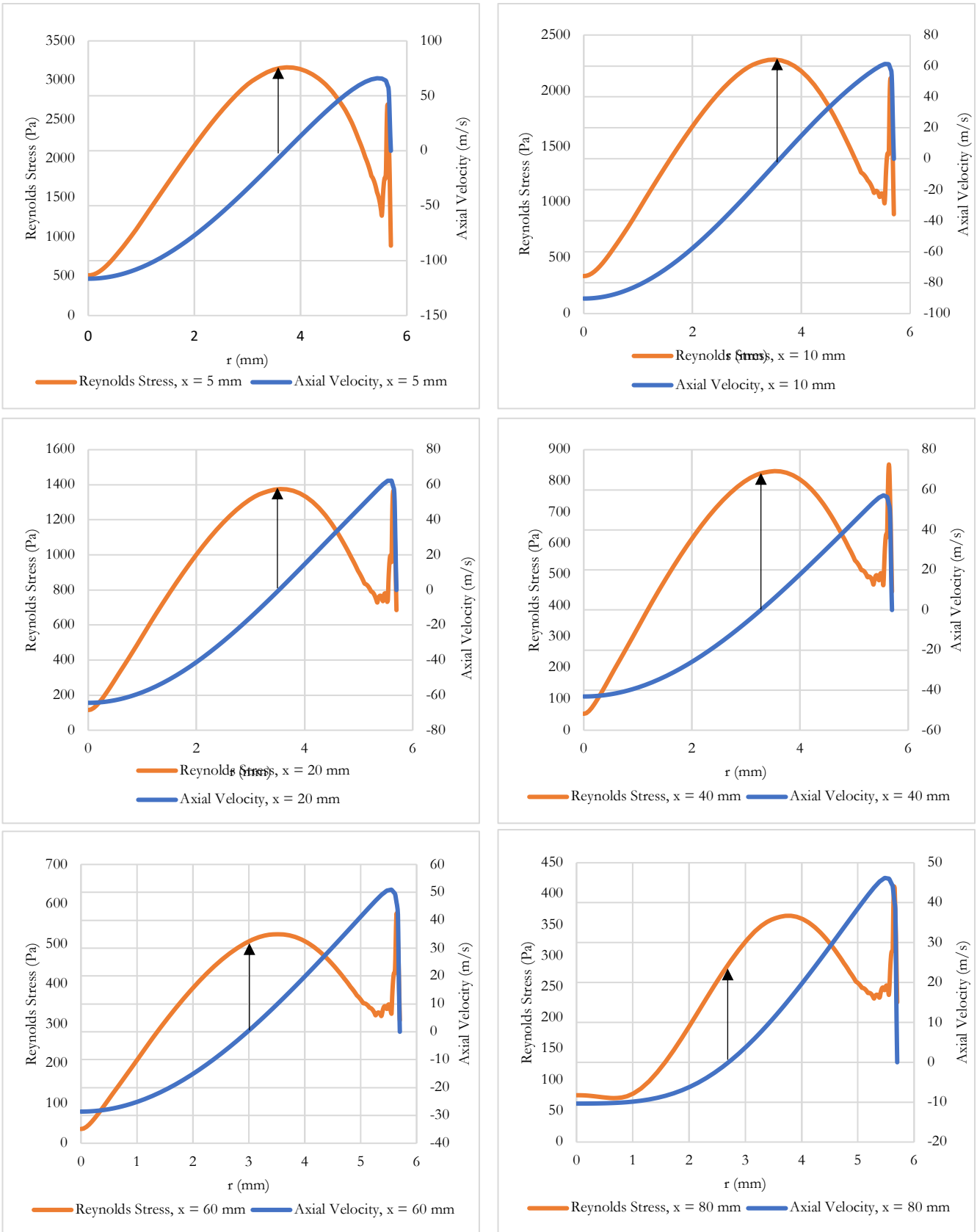

Figure 28. Reynolds Stress and axial velocity at various axial locations

8.2.4 Energy contained in the flow

The energy contained in any flow can be divided into three parts. The energy contained in the form of temperature i.e. the enthalpy of the flow, and the mean kinetic and turbulent kinetic energies present in the flow. The sum of these is also called the Total Enthalpy or the Total Energy of the flow. In a vortex tube, a total temperature separation is observed as we move radially from the core to the annular region which signifies an energy separation phenomenon being present in the flow. But the mechanisms responsible for the core flow to lose its energy and the annular flow to gain its energy can be deduced by looking at the individual components that make up the flow energy.

Static temperature curve shown in fig. 29 shows an interesting behavior where the static temperature is constant in the core region and then starts to drop in the transition zone and then again increasing in the annular region finally reaching very high values near the wall. Static temperature being almost a constant through most of the tube radius signifies that there is heat diffusion radially throughout the flow.

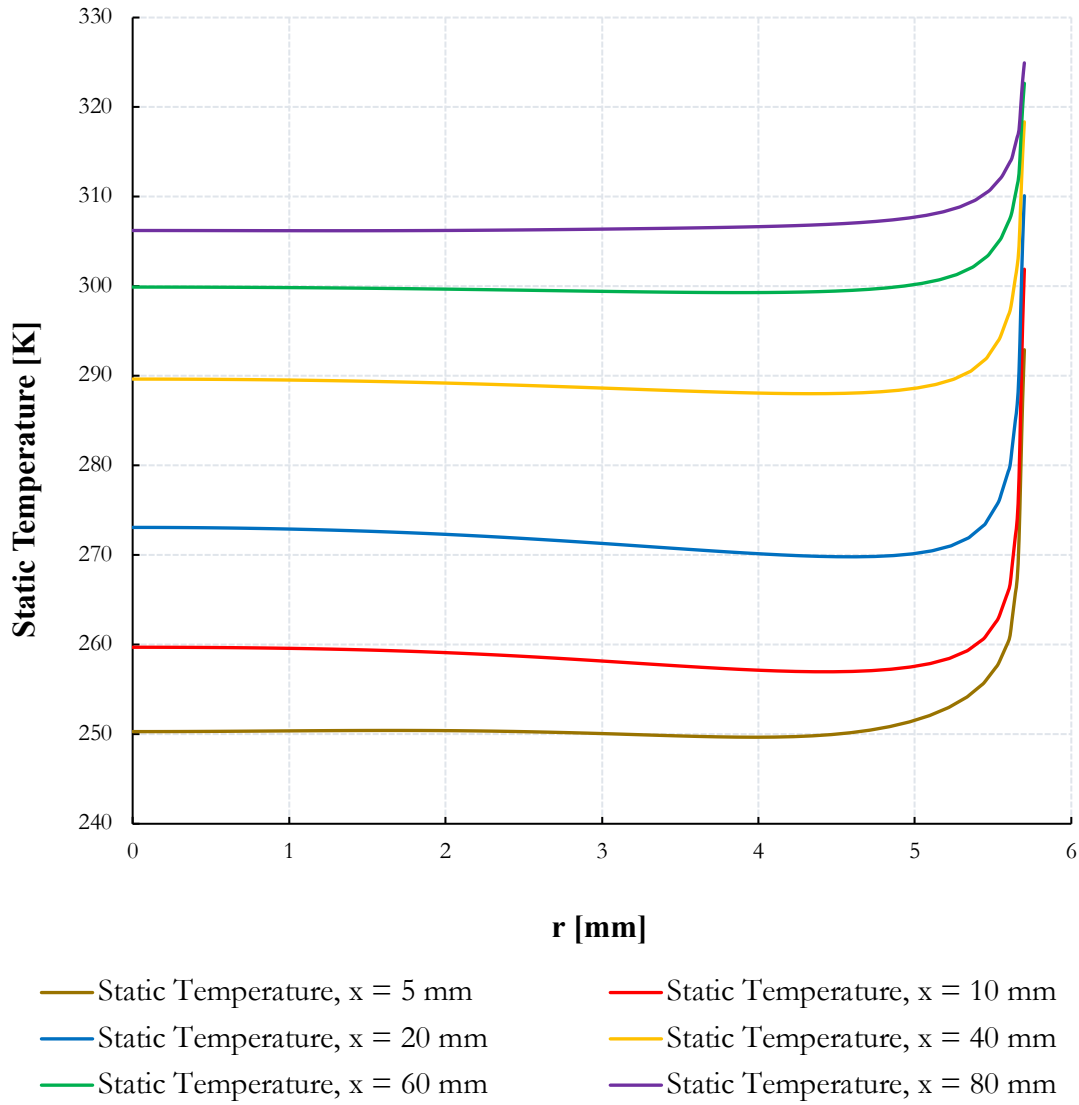

Figure 29. Static Temperature distribution at various axial locations

Comparing the static and total temperatures from the fig. 29 and 30, it is observed that as we move along the radius away from the core, the energy contained in the fluid is mainly the kinetic energy of the flow. This is seen from the deviation of the total temperature from the static temperature. Thus, the region very close to the vortex tube center i.e. the core flow is dominated by internal energy whereas the flow away from the center is dominated by kinetic energies of the mean flow and the turbulence.

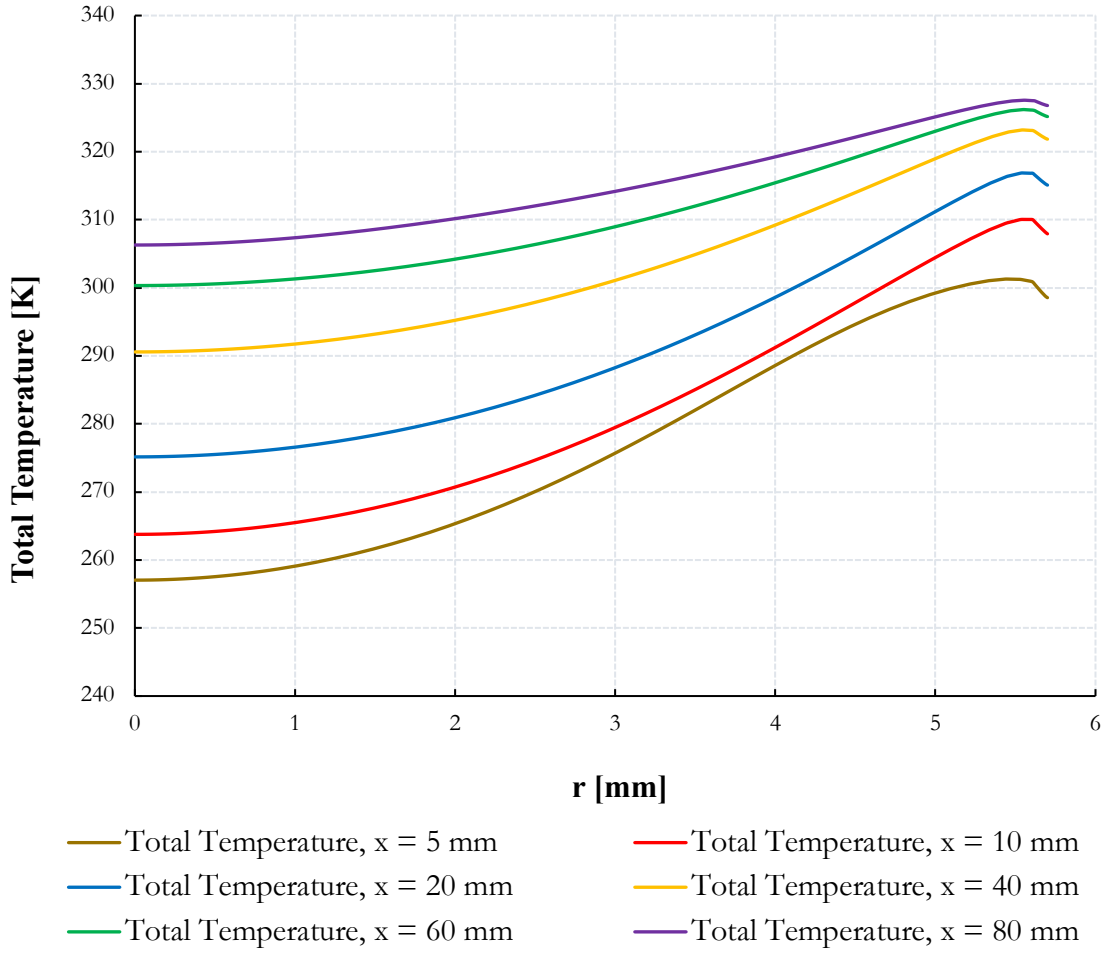

Figure 30. Total Temperature distribution at various axial locations

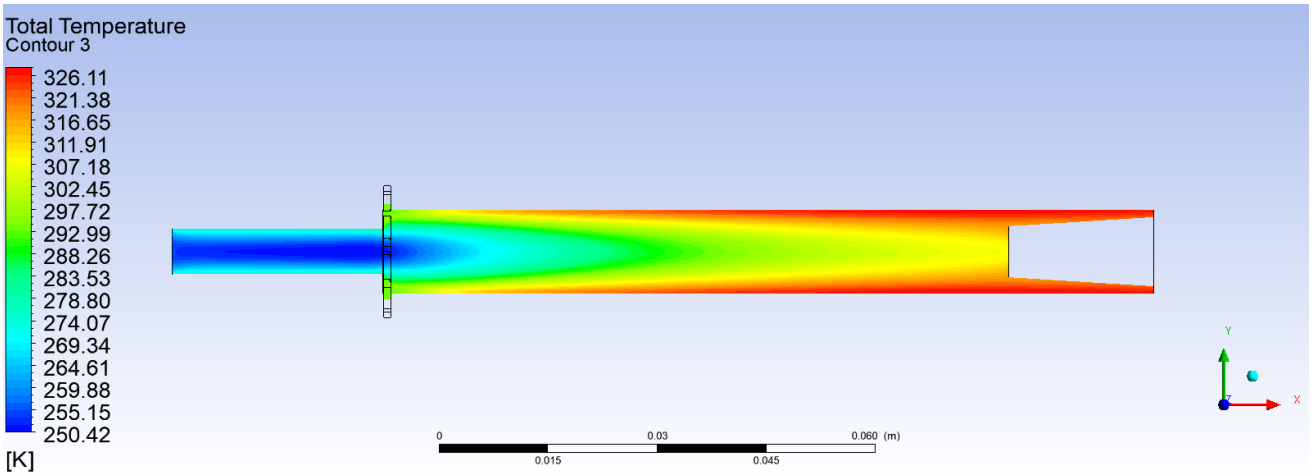

Figure 31. Total temperature contour inside the vortex tube

Looking at the total enthalpy of the flow field an idea on how the energy is being distributed radially across the flow is apparent.

$$h_T = \rho \left(c_P T + \frac{1}{2} V^2 + \frac{3}{2} (\overline{(u')^2}) \right) \tag{21}$$

Specifically, the total enthalpy indicates that the energy contained in the flow as a combination of static temperature, mean flow kinetic energy and the turbulence kinetic energy.

We can see that the total energy of the flow in fig. 32, if compared between the different axial locations, shows an energy increase at the lower portions of the radius and eventually crosses over and begins to drop as the wall is approached.

The axial velocity cross-over point where the flow changes direction lies between a radial location of 2.6 - 3.7 mm as observed from the axial velocity plot shown in fig 21. According to our previous analysis, the flow is characterized by core region, followed by a transition region, and then a free vortex region which exists above this cross-over point. Thus, the observed drop in flow energy is located in the region of the free vortex. As previously shown in the comparison between the total and static temperatures, this region is dominated by the flow kinetic energy. Hence, the energy drop can be related to the loss of kinetic energy (both mean and turbulent) of the flow.

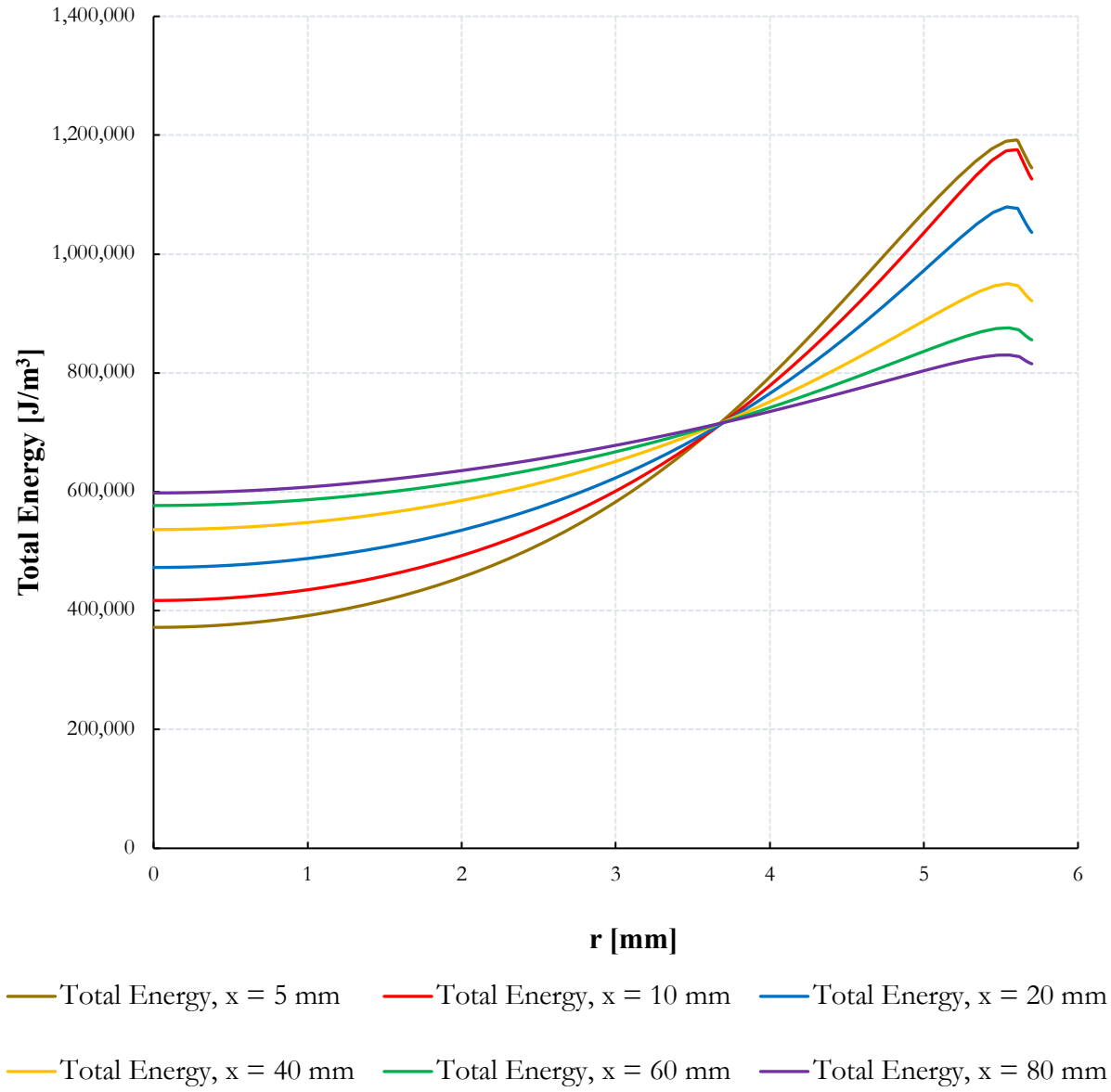

Figure 32. Total Energy distribution at various axial locations

The total temperature at the vortex tube wall i.e. the total temperature of the annular flow shown in fig. 33 reaches a maximum at an axial location of approximately x = 86 mm. This is where the hot control valve begins, and all the cold flow has reversed. The flow energy profile in fig. 32 also shows that the energy gradient between the core and annular flows drops as we move towards the hot exit. At x=80mm, the energy profile is almost flat. Thus, following this trend it can be safely assumed that

the total energy difference between the core and annular flow becomes very small as we move further downstream and thus the temperature in the annular flow has reached a constant value because there is no gradient causing a transfer of energy between the two flows.

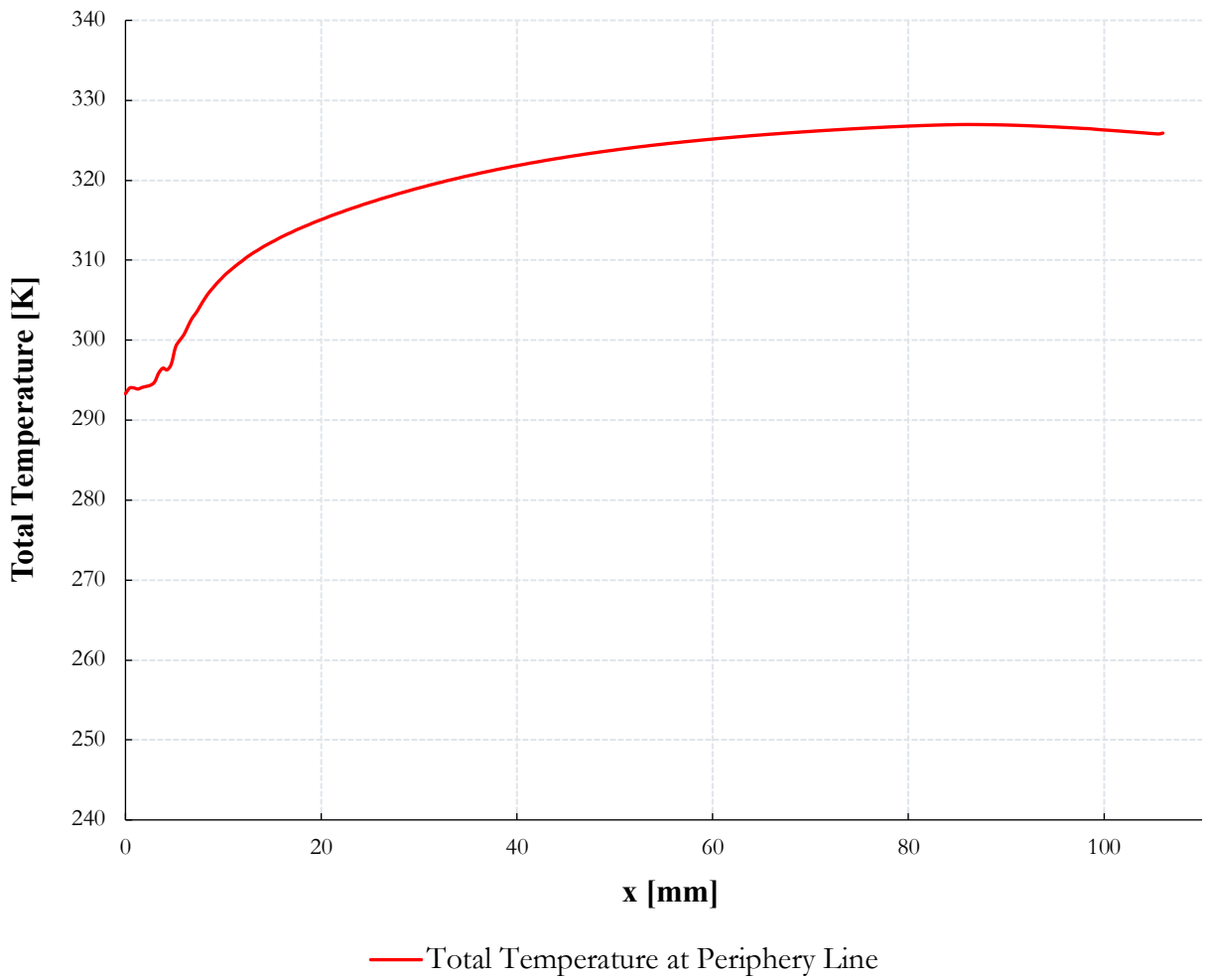

Figure 33. Total Temperature at Vortex tube periphery

8.3 Analysis of Cold Flow

It was initially though that the temperature drop at the cold occurred because of the expansion of the high-pressure gas at the inlet directly expanding and leaving the cold exit. This led to the conclusion that the flow reversing from the hot section was deteriorating the performance of the vortex tube by mixing with the cold flow that is directly expanding from the inlet. In order to confirm this, it must be demonstrated that a part of the cold mass directly expands from the inlet into the low-pressure region at the vortex tube center. Calculating the cold mass flow in the cross-sectional plane at the inlet is not so accurate because there is no possibility of differentiating the cold mass directly expanding from the inlet to the cold mass that is reversing from the hot section of the vortex tube. Thus, in this study, a plane was created just outside the inlet nozzles and towards the hot section. The mass flow rate of the hot flow (gas flowing towards the hot exit) was calculated and the difference between the inlet mass flow rate and the hot mass flow rate at this plane will provide the cold mass flow that is directly expanding from the inlet into the core region.

The hot mass flow calculated for this section is $\dot{m} = 0.010\ kg/s$ which is the total mass flow at the inlet. Thus, the cold flow is starting the reverse after it has travelled into the hot section of the tube, and only an insignificant amount is expanding directly into the low-pressure region in the center of the vortex tube.

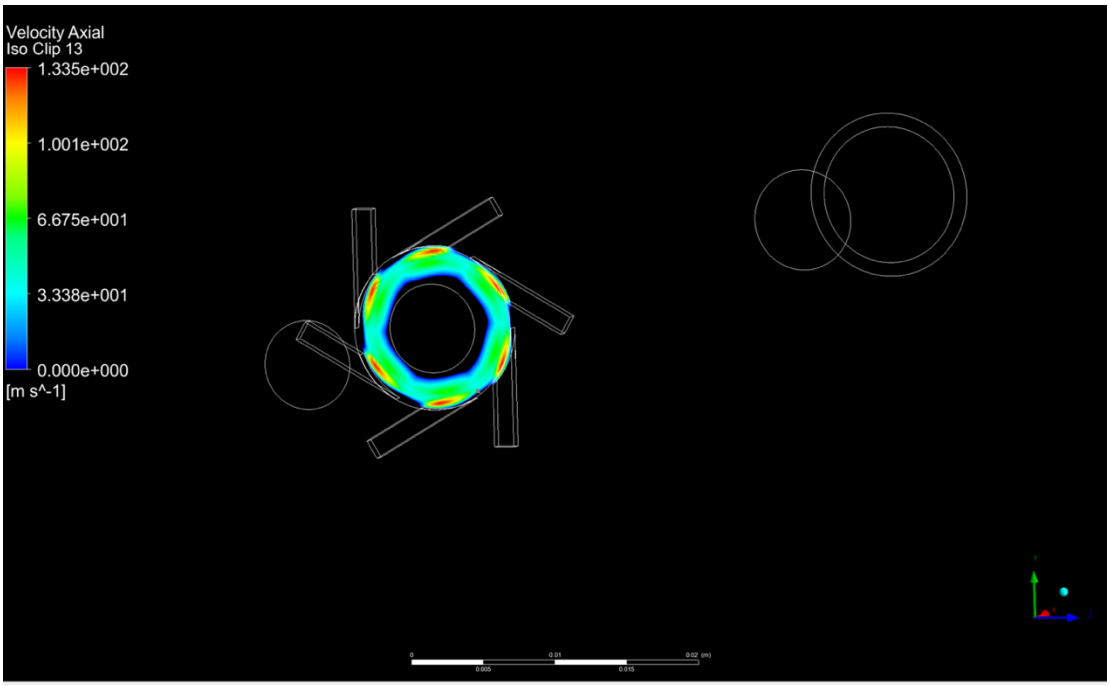

Figure 34. Hot flow just outside the inlet section

Temperature at the core of the vortex tube will provide some insight into the process that is taking place. The following fig. 34 shows the comparison between the actual static temperature obtained from the computational analysis and the calculated isentropic expansion temperature at the vortex tube centerline i.e. core flow. The pressures were obtained from the computation.

The temperature ratio for an adiabatic flow is given by,

$$\frac{T_2}{T_1} = \left(\frac{P_2}{P_1}\right)^{\left(\frac{\gamma - 1}{\gamma}\right)} \tag{22}$$

Where $\gamma = 1.4$ is the ratio of specific heats for air. Using this formula, the isentropic temperature drop resulting from the expansion was calculated at the vortex tube centerline for the cold flow.

Fig. 35 is by far the most interesting result as the actual temperature is lower than the calculated isentropic temperature which signifies the presence of energy transfer through either work, heat or both that took place between the reversing core flow and annular hot flow.

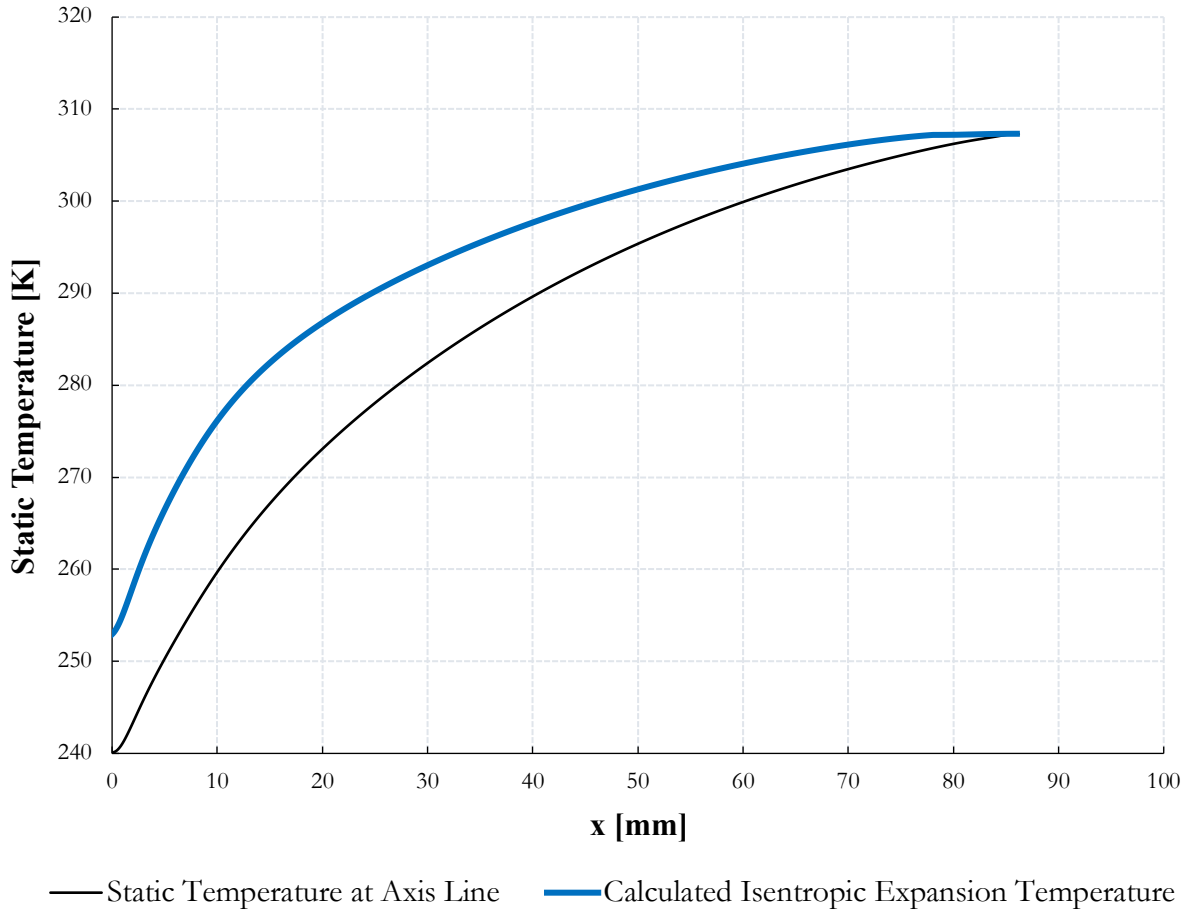

Figure 35. Static Temperature at the centerline of the vortex tube

8.3.1 Control Volume Analysis of Cold Flow

In order to support the idea that there is an energy transfer between the cold and hot flows by means of both heat and work transfer, a control volume analysis was performed on the cold flow. From the analysis of axial velocities, we have determined the cold flow is the part of the flow where the axial

velocity is negative (according to the current model) in the central region of the vortex tube also referred to as the core region, and the interface highlighted by zero axial velocity is the cross-over point where the flow reversal happens. The cross-over points were plotted at discrete axial locations and was found to be a linearly decreasing profile and an equation was obtained using linear fit shown in fig. 22. This line was revolved to obtain the control volume for the cold flow. A 2D representation of the control volume is shown in the fig. 36.

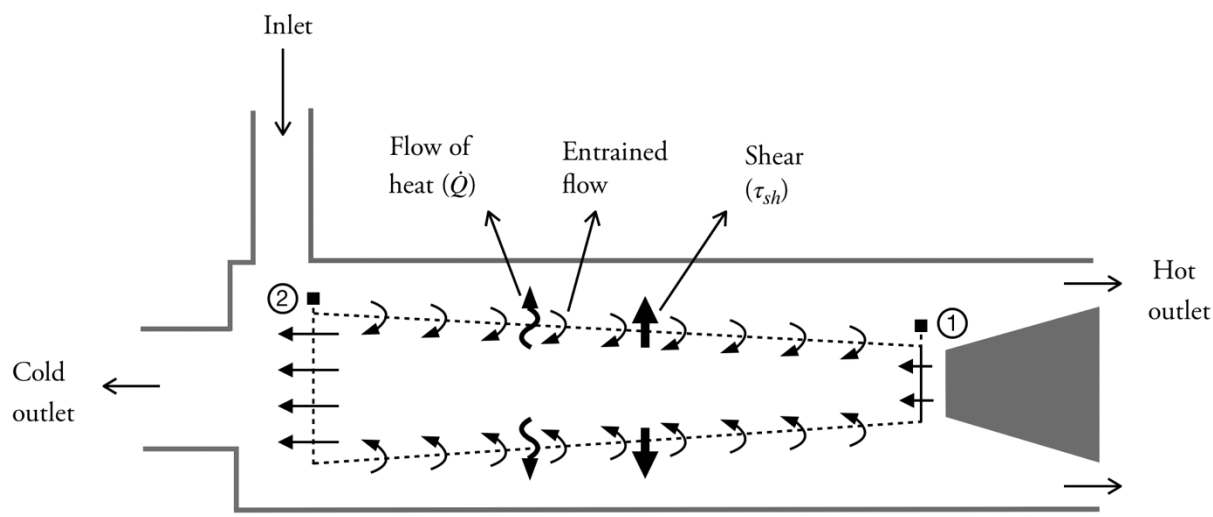

Figure 36. Control Volume of Cold Flow

The following assumptions were made during the application of the energy analysis to the Control Volume. (a) The flow is steady state (implicitly factored in during the CFD analysis phase itself) and (b) The flow is axisymmetric. Applying the first law for an open system gives,

$$\frac{dE_{CV}}{dt} = \Delta Q + \Delta W + \sum_{in} \dot{m} h_T - \sum_{out} \dot{m} h_T \tag{23}$$

According the assumption (1), there is no change in the energy inside the CV with respect to time ($dE_{CV} \ / \ dt = 0$). Thus eq. (11) becomes,

$$\sum_{out} \dot{m} h_T - \sum_{in} \dot{m} h_T = \Delta Q + \Delta W \tag{24}$$

The CV of the cold flow can be considered as one with multiple inlet ports and a single exit port. This is the flow that is entrained into the core region and reversed continuously as the flow moves down towards the hot exit of the vortex tube, and therefore is similar to a system with multiple inlets. But all of this flow leaves the CV through the cold orifice, thus allowing for a single outlet.

$$\dot{m}_{in} = \dot{m}_1 + \dot{m}_{entrained} \tag{25}$$

$$\sum_{out} \dot{m} h_T - \sum_{in} \dot{m} h_T = \sum_{2} \dot{m} h_T - (\sum_{1} \dot{m} h_T + \sum_{entrained} \dot{m} h_T) \tag{26}$$

The mass flow entrained within the control volume at a particular section was computed by calculating the mass flow rate difference in the hot flow before and after that particular section. A collection of such sections with a small interval of Δx shown in fig. 37, were used to approximate the mass flow rate of the entrained flow.

$$\dot{m}_{entrained,i} = \dot{m}_{hot,i} - \dot{m}_{hot,i+1} \tag{27}$$

The total enthalpy at the control surface was obtained directly from the simulation. Thus, in order for the total energy calculation to be accurate, the Δx between the two planes used to compute the entrained mass flow rate had to be very small. To achieve this effect approximately 800 planes were created using scripting in CFX-Post and the mass flow rate at all the planes were determined. The final plane at section 1 lies in the region where more than 95% of the cold mass has reversed. We don't see a stagnation point in terms of centerline axial velocity in the current simulation, hence we take this criterion to define the stagnation zone in the current analysis.

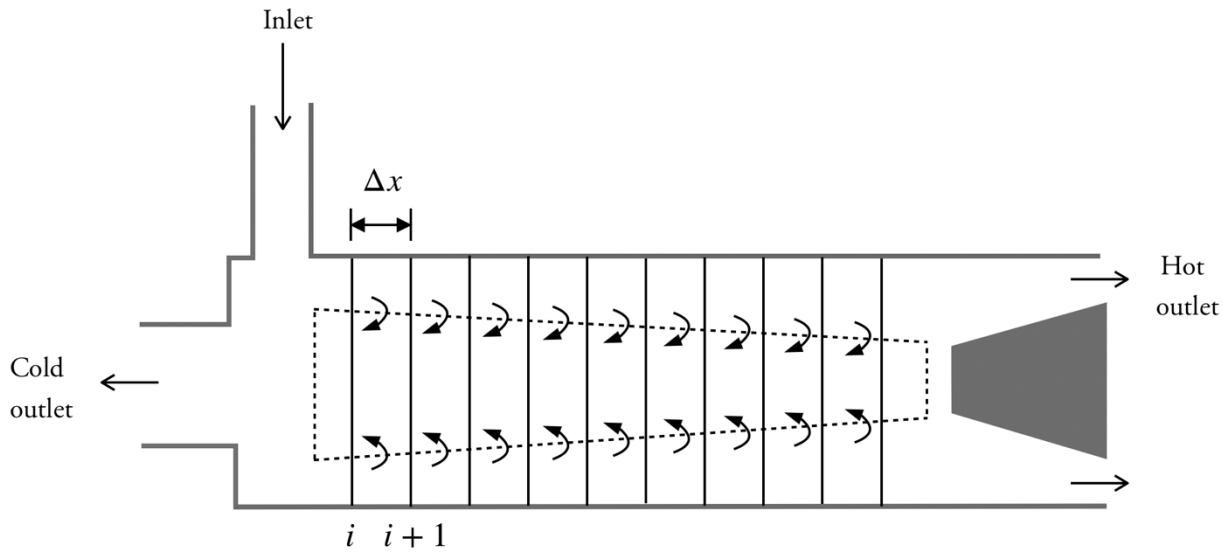

Figure 37. Planes to calculate the entrained mass

Section 2 is defined as the location immediately downstream of the inlet. We do not take it as the entrance of cold orifice because the complicated flow features at the inlet make it difficult to assume the work and heat transfer in the region. With the mass flow rates at the different axial locations and the total enthalpies obtained, the total energy entering and leaving the CV was calculated.

Table 3. Calculating of the flow energy entering and leaving the control volume

Location	*Mass flow rate (kg/s)*	*Flow Energy (W)*
Section 1	0.000259	80.76
Entrained flow	0.004976	1445.71
Section 2	0.004999	1339.69
Total Energy difference		-186.78

From Table 1 it can be seen that the flow loses energy (i.e., the negative sign) as it comes out of the CV thus signifying that there is loss of energy through other mechanisms such as heat and work transfer in addition to the expansion.

8.3.2 Calculating heat and work transfers

Both heat and work transfer are present between the cold and the hot flows [4]. For turbulent flows like the one present in vortex tube, turbulent transfer of heat dominates over the diffusion by molecular processes and can be approximated by the following eq. (16). Here the gradient of the temperature at the boundary of the CV was used. The radial gradient (gradient along y-direction) was taken because there is only radial flow of heat between the core and the annular flows. In our assumption of the control volume, we took the axial velocity as the criteria to determine the CV boundary. But we did not confirm if this is the primary location where the heat transfer took place. In order to confirm this, the temperature gradient along the radius was analyzed which is shown in fig. 38.

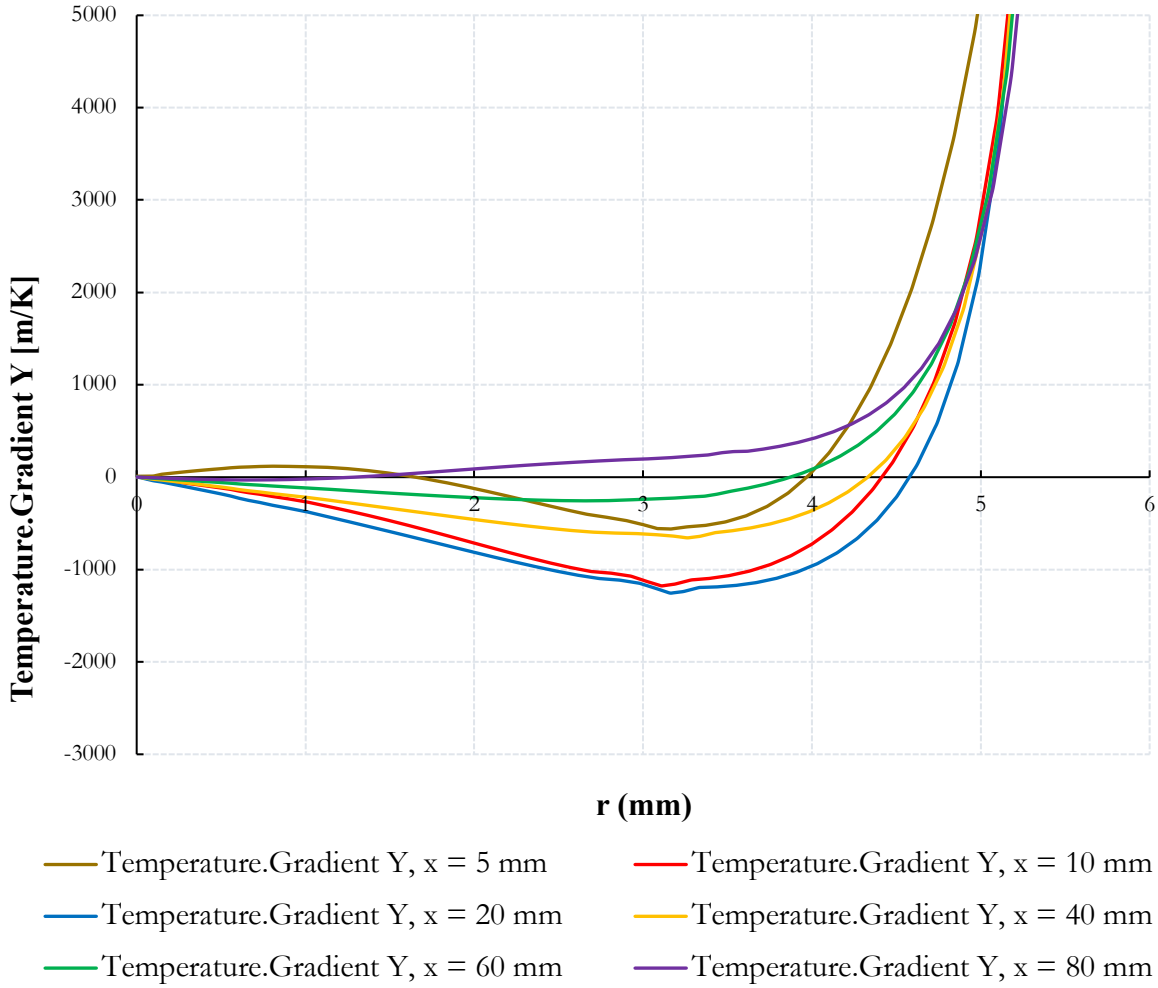

Figure 38. Temperature Gradient in y-direction at different axial locations

From the fig. 38, we can define the boundary as the location where the temperature gradient changes character i.e. it goes from a decreasing gradient to an increasing gradient. This signifies the presence of a heat exchange at this location. If we compare the radial location of these points, they lie in the radius of 3.1-3.3mm for the axial locations of x=5, 10, 20 and 40 mm and for x=60 mm it lies at 2.6 mm all of which agree well with the axial velocity cross-over points in these regions. Thus, the definition of our control volume boundary seems to be validated.

Heat transfer is primarily caused by the eddies generated by the shear at the cross-over region. In such a case, the heat transfer can be calculated by the conduction equation but with the turbulent conductivity as the proportionality factor.

$$\dot{q} = \left(k + \frac{c_p \mu_t}{Pr_t}\right)\frac{\partial T}{\partial y} \tag{28}$$

Where the term in the bracket is the effective thermal conductivity which is a combination of both molecular and turbulent thermal conductivities. The Turbulent Prandtl number is given by,

$$Pr_t = \frac{\mu_t}{\lambda_t} \tag{29}$$

$$\dot{Q} = \oint \dot{q}\, ds \tag{30}$$

Work transfer is a combination of shear at the control surface and work done in the expansion of cold fluid between sections 1 and 2. Shear can be calculated using eq. (31). The term ($\mu_t + \mu$) is called the effective viscosity which is the sum of turbulent (i.e., eddy) and molecular viscosities. But since in the shear layer (cross-over region) turbulence dominates, eddy viscosity is the dominant term ($\mu_t \gg \mu$). The shear can be viewed as a retarding force produced by the core flow and acting on the annular flow, as they both rotate and the tangential velocity (velocity w) is the component of velocity acted upon by the shear at the cross-over region. Hence, the tangential velocity gradient along the radius (y-direction) is used in the calculation of shear.

$$\tau_{sh} = (\mu_t + \mu)\frac{\partial w}{\partial y} \tag{31}$$

$$\dot{W}_{sh} = \oint (\tau_{sh}\, w)\, d\, s \tag{32}$$

As the flow reverses and moves towards the cold exit, it expands having a total pressure drop as it flows. This is the work done because of the flow expansion between the sections 1 and 2 and must be factored in the work equation.

$$\dot{W}_{exp,1-2} = \int_1 (P_T\, u)\, d\, A - \int_2 (P_T\, u)\, d\, A \tag{33}$$

$$\dot{W} = \dot{W}_{sh} + \dot{W}_{exp,1-2} \tag{34}$$

Heat and work transfers are in the form of rates. But in table 4 we mention it as $\Delta Q + \Delta W$ just to be consistent in notation with the eq. 23 & 24.

Table 4. Calculating of the work and heat transfer at the control surface

Property	***Value (W)***
Heat flow ($\dot{Q}$)	34.9
$\dot{W}_{sh}$	582.67
$\dot{W}_{exp,1-2}$	-445.64 (= 23.56 - 469.20)
$\Delta Q + \Delta W$	171.94

Comparing the values from Tables 3 and 4, we can see that the total energy difference between the incoming and outgoing cold flow and the amount of energy flowing out of the CV through the

assumed heat and work processes are in good agreement with a difference less than 10% thus supporting the proposed concept model.

The above Table 4 can also give some insight into the various processes that create the cold flow inside the vortex tube. It is also shown that the heat transfer has a negative sign which indicates that heat is flowing out of the CV. Thus, the eddies formed due to shear carry the heat away from the core. This is an interesting result, which is confirmed in the static temperature curve (fig. 29), where a reduction in temperature between the core and transition region is observed. The significant work transfer term is a result of the turbulent shear work done by the cold flow on the hot flow.

9. Conclusion and Future Work

The computational analysis of the flow properties and an explanation for energy separation observed inside a counter-flowing Ranque-Hilsch Vortex Tube has been performed using a RANS based two-equation turbulence model $Std\ k - \varepsilon$. The model was intially validated using experimental results and the agreement was found to be very good in terms of the total temperature predictions at the hot and cold end. A comparison of the flow properties i.e. the tangential, axial velocity and the static temperature profiles was made with a published computational research which used higher order LES model and this provided insight into the differences between the various turbulence models. The $Std\ k - \varepsilon$ predicted a qualitatively different flow profile for the tangential velocity with a different distribution of the free, transition and forced vortex region when compared to the LES. The LES predicted a forced vortex region only up to a radial location y/R of 0.25, then a transition region and a free vortex region whose size with respect to radius increased with an increase in the axial distance from the inlet. Whereas the $Std\ k - \varepsilon$ model predicted an overly diffusive tangential velocity profile with the forced vortex extending up to a y/R of 0.7 and then the free vortex region came very close to the wall at a y/R of 0.92. The behavior was the same for all the axial locations with the magnitude of the tangential velocity itself dropping in further downstream locations. The axial velocities predicted by the LES research had a bit of a non-linear characteristic in both the forced and the free vortex region but the $Std\ k - \varepsilon$ model predicted an almost linearly increasing axial velocity profiles in both the regions. Static temperature profile predicted by $Std\ k - \varepsilon$ remained fairly constant almost in the entire radius at a particular axial location and increased very close to the wall. With the strengths and drawbacks of the $Std\ k - \varepsilon$ model in mind, the other flow properties were looked in detail.

Vorticity results from the model confirmed the presence of a forced vortex region at the core with the vorticity being constant in the forced vortex region, dropping to zero in the annular region and then increasing exponentially in the region close to the wall because of the presence of a boundary layer. The strain rate curves showed a very low strain rate in the central region and increasing with the radius. There was a presence of an inflection point in the central regions of the radius where the gradient of the rise dropped and then another inflection point appeared at the annular region where the values increased exponentially till the wall. The Reynolds Stress which was calculated using the Boussinesq hypothesis was found to agree well with our expectations with the presence of high shear in the cross-over region i.e. the interface between the two counter-flowing fluid streams. But it was found to have an overly diffusive profile caused by the eddy viscosity as the Reynolds Stress is a combination of both the eddy viscosity and strain rate. This was expected as the two-equation isotropic models like the $Std\ k - \varepsilon$ are expected to calculate an overly diffusive eddy viscosity profile because they neglect the effect the swirl has on the dampening of the turbulent stresses.

Explanation for the energy separation phenomenon was then attempted. The distribution of the flow energy was studied, and it was observed that an energy separation was present between the core and annular flows causing a temperature drop and rise respectively in the two flows. The Reynolds stress validated our assumption that it was maximum at the cross-over region, the interface between the core and annular flows. This Reynolds stress gives rise to turbulence which breaks down in the near wall region causing a rise in temperature of the annular flow. Using a control volume energy analysis on the cold flow, the dominant mode of energy transfer between the cold and hot flows was identified. It was found that the tangential shear between the cold and hot flows was the dominant component of work. Further the thermal energy transferred in that region when compared to the energy transfer

due to shear stress work was only a fraction of the amount. Thus, this thesis comprehensively covers all the important aspects of vortex tube flow and also the energy separation observed.

Now having an idea about the phenomenon, future work on how to enhance the temperature separation effect for a given pressure ratio can be studied. Some other works would include:

- Running higher order models like RSM and LES to simulate the flow more accurately and identify the particular components of the turbulent stresses that have the maximum effect.

- Since the turbulence stresses significantly impact energy separation, mechanism to increase the turbulence and hence the shear at the cross-over region can be looked at [21].

Some other works that can be performed based on recent developments include:

- Performing a Design of Experiments (DOE) with the various parameters of the vortex tube like the pressure ratio and other geometrical parameters, to come up with a Response Surface of the output variable with respect to the independent variables. From this a sensitivity analysis can be performed to identify the parameter that has the maximum effect on the temperature separation effect and vice versa.

- Constructing ANNs (Artificial Neural Networks) to incorporate more independent variables into the system and to increase the predictive efficiency of the network by capturing the relationship between the independent variables.

References

[1] J. P. Harnett and E. R. G. Eckert, "Experimental Study of the Velocity and Temperature Distribution in a High-Velocity Vortex-Type Flow," *Trans. ASME*, vol. 79, no. 4, pp. 751–758, 1957.

[2] H. H. Brunn, "EXPERIMENTAL INVESTIGATION OF THE ENERGY SEPARATION IN VORTEX TUBES," *J. Mech. Eng. Sci.*, vol. 11, no. 6, pp. 567–582, 1969.

[3] R. G. Deissler and M. Perlmutter, "Analysis of the flow and energy separation in a turbulent vortex," *Int. J. Heat Mass Transf.*, vol. 1, no. 2–3, pp. 173–191, 1960.

[4] V. Deemter, "On THE THEORY OF THE RANQUE-HILSCH COOLING EFFECT," *Appl. Sci. Res.*, vol. 3, pp. 174–196.

[5] Y. Xue, M. Arjomandi, and R. Kelso, "Experimental study of the flow structure in a counter flow Ranque-Hilsch vortex tube," *Int. J. Heat Mass Transf.*, vol. 55, no. 21–22, pp. 5853–5860, 2012.

[6] Y. Xue, M. Arjomandi, and R. Kelso, "Energy analysis within a vortex tube," *Exp. Therm. Fluid Sci.*, vol. 52, pp. 139–145, 2014.

[7] B. Ahlborn and S. Groves, "Secondary flow in a vortex tube," *Fluid Dyn. Res.*, vol. 21, no. 2, pp. 73–86, 1997.

[8] B. K. Ahlborn and J. M. Gordon, "The vortex tube as a classic thermodynamic refrigeration cycle," *J. Appl. Phys.*, vol. 88, no. 6, pp. 3645–3653, 2000.

[9] H. Takahama and H. Yokosawa, "Energy Separation in Yerfei Tubes with a Divergent Chamber," *J. Heat Transfer*, vol. 103, no. May, pp. 196–203, 1981.

[10] P. A. Ramakrishna, M. Ramakrishna, and R. Manimaran, "Experimental investigation of

temperature separation in a counter-flow vortex tube," *J. Heat Transfer*, vol. 136, no. 8, pp. 1–6, 2014.

[11] D. Stephan, K; Lin S; Durst, M; Huang, F; Seher, "AN INVESTIGATION OF ENERGY SEPARATION IN A VORTEX TUBE," *Int. J. Heat Mass Transf.*, vol. 26, no. 3, pp. 341–348, 1983.

[12] Y. Xue, M. Arjomandi, and R. Kelso, "The working principle of a vortex tube," *Int. J. Refrig.*, vol. 36, no. 6, pp. 1730–1740, 2013.

[13] W. Fröhlingsdorf and H. Unger, "Numerical investigations of the compressible flow and the energy separation in the Ranque-Hilsch vortex tube," *Int. J. Heat Mass Transf.*, vol. 42, no. 3, pp. 415–422, 1998.

[14] J. J. Keyes, Jr., "An Experimental study of gas dynamics in high velocity vortex flow," *Proc. Heat Transf. Fluid Mech. Inst.*, pp. 31–46, 1960.

[15] S. Eiamsa-ard and P. Promvonge, "Numerical investigation of the thermal separation in a Ranque-Hilsch vortex tube," *Int. J. Heat Mass Transf.*, vol. 50, no. 5–6, pp. 821–832, 2007.

[16] T. Dutta, K. P. Sinhamahapatra, and S. S. Bandyopdhyay, "Comparison of different turbulence models in predicting the temperature separation in a Ranque-Hilsch vortex tube," *Int. J. Refrig.*, vol. 33, no. 4, pp. 783–792, 2010.

[17] T. Dutta, K. P. Sinhamahapatra, and S. S. Bandyopadhyay, "CFD Analysis of Energy Separation in Ranque-Hilsch Vortex Tube at Cryogenic Temperature," *J. Fluids*, vol. 2013, pp. 1–14, 2013.

[18] N. Bej and K. P. Sinhamahapatra, "Numerical analysis on the heat and work transfer due to shear in a hot cascade Ranque-Hilsch vortex tube," *Int. J. Refrig.*, vol. 68, pp. 161–176, 2016.

[19] N. F. Aljuwayhel, G. F. Nellis, and S. A. Klein, "Parametric and internal study of the vortex tube using a CFD model," *Int. J. Refrig.*, vol. 28, no. 3, pp. 442–450, 2005.

[20] A. Secchiaroli, R. Ricci, S. Montelpare, and V. D'Alessandro, "Numerical simulation of turbulent flow in a Ranque-Hilsch vortex tube," *Int. J. Heat Mass Transf.*, vol. 52, no. 23–24, pp. 5496–5511, 2009.

[21] V. Bianco, A. Khait, A. Noskov, and V. Alekhin, "A comparison of the application of RSM and les turbulence models in the numerical simulation of thermal and flow patterns in a double-circuit Ranque-Hilsch vortex tube," *Appl. Therm. Eng.*, vol. 106, pp. 1244–1256, 2016.

[22] T. Farouk and B. Farouk, "Large eddy simulations of the flow field and temperature separation in the Ranque-Hilsch vortex tube," *Int. J. Heat Mass Transf.*, vol. 50, no. 23–24, pp. 4724–4735, 2007.

[23] A. G. Rajagopalan and P. J. Disimile, "Geometric Modifications and Their Impact on the Performance of the Vortex Tube," no. 3, pp. 1–12, 2015.

[24] H. R. Thakare, A. Monde, and A. D. Parekh, "Experimental, computational and optimization studies of temperature separation and flow physics of vortex tube: A review," *Renew. Sustain. Energy Rev.*, vol. 52, pp. 1043–1071, 2015.

[25] A. R. Bramo and N. Pourmahmoud, "Computational fluid dynamics simulation of length to diameter ratio effects on the energy separation in a vortex tube," *Therm. Sci.*, vol. 15, no. 3, pp. 833–848, 2011.

[26] O. Uluer, V. Kirmaci, and Ş. Ataş, "Using the artificial neural network model for modeling the performance of the counter flow vortex tube," *Expert Syst. Appl.*, vol. 36, no. 10, pp. 12256–12263, 2009.

[27] K. Dincer, S. Tasdemir, S. Baskaya, and B. Z. Uysal, "Modeling of the effects of length to diameter ratio and nozzle number on the performance of counterflow Ranque-Hilsch vortex tubes using artificial neural networks," *Appl. Therm. Eng.*, vol. 28, no. 17–18, pp. 2380–2390, 2008.

[28] F. Kocabas, M. Korkmaz, U. Sorgucu, and S. Donmez, "Modeling of heating and cooling performance of counter flow type vortex tube by using artificial neural network," *Int. J. Refrig.*, vol. 33, no. 5, pp. 963–972, 2010.

[29] H. M. Skye, G. F. Nellis, and S. A. Klein, "Comparison of CFD analysis to empirical data in a commercial vortex tube," *Int. J. Refrig.*, vol. 29, pp. 71–80, 2006.

[30] R. Biswas and R. C. Strawn, "Tetrahedral and hexahedral mesh adaptation for CFD problems," *Appl. Numer. Math.*, vol. 26, no. 1–2, pp. 135–151, 1998.

[31] W. C. Contributors, "Law of the wall," *https://commons.wikimedia.org/w/index.php?title=File:Law_of_the_wall_(English).svg&oldid=197442076*, 2016. .

[32] M. P. Escudier and J. J. Keller, "Recirculation in swirling flow: A manifestation of vortex breakdown," *AIAA J.*, vol. 23, no. 1, pp. 111–116, 1985.

[33] ANSYS FLUENT 13 User's Guide, *Ansys Fluent Theory Guide*, vol. 15317, no. November. 2013.

[34] M. G. D. Fokke, T. L. Liem, J. J. Derksen, and H. E. A. Van Den Akker, "LDA and LIF Experiments on the quasi-periodic and complex flow in a cyclone," in *7th Int. Symposium on Applications of Laser Techniques to Fluid MechanicsAt*, 1994, no. July.

[35] J. C. Chen and C. a Lin, "COMPUTATIONS OF STRONGLY SWIRLING FLOWS WITH SECOND-MOMENT CLOSURES," *Int. J. Numer. Methods Fluids*, vol. 30, pp. 493–508, 1999.

[36] S. Hogg and M. A. Leschziner, "Computation of Highly Swirling Confined Flow with a Reynolds Stress Turbulence Model," *AIAA J.*, vol. 27, no. 1, pp. 57–63, 1989.

[37] D. C. Wilcox, *Turbulence Modeling For CFD*, 2nd ed. DCW Industries inc., 1993.

[38] J. J. Derksen and H. E. A. Van Den Akker, "Simulation of vortex core precession in a reverse-flow cyclone," *AIChE J.*, vol. 46, no. 7, pp. 1317–1331, 2000.

[39] F. Chang and V. K. Dhir, "Turbulent flow field in tangentially injected swirl flows in tubes,"

Int. J. Heat Fluid Flow, vol. 15, no. 5, pp. 346–356, 1994.